Hydrology and Quantitative
Water Management Group (HWM)
WAGENINGEN, THE NETHERLANDS

MASTER EARTH AND ENVIRONMENT (MEE)

THESIS

Tidal influence on the discharge distribution at two junctions of the Kapuas River (West Kalimantan, Indonesia)

Supervisors:
Dr. Ir. A.J.F Hoitink
Karl Kästner MSc.

David Fernando Muñoz Pauta
900310593130

January 25, 2017

Abstract

Tides influence the allocation of river discharge to channels interconnected by tidal junctions. Model simulations on the Kapuas Delta in Indonesia reveal how under idealized river discharge conditions, the discharge distribution is controlled by the tidal behavior at the junctions. The hydrodynamic model consisted of the main branch of the Kapuas and two side channels, and was used to simulate the tidal motion at high and low constant river discharge. At low river flow, the tidal motion has a strong influence on the discharge distribution at both junctions. At high river flow, however, the effect of the tides in river discharge is weak. Analysis of the tidal energy fluxes at the junctions indicates that at the downstream junction, the Kubu channel continuously adds tidal energy to the river system. The upstream junction, on the other hand, drains or adds tidal energy to the main river, depending on the river discharge. A sensitivity analysis of tidal attenuation and discharge distribution is performed by evaluating a set of fifty scenarios, with varying river discharge, bed roughness and mean bed level. In general, high bed roughness values enhance tidal damping in the channels and allocate the river discharge to the river branches. When the river discharge increases, less river discharge is allocated to the main channel and more tidal damping is observed in the Kapuas. Bed level variation in the simulations has limited influence on tidal attenuation and the associated discharge distribution.

Keywords:

Kapuas River, river discharge-tide interaction, tidal junction, tidal energy flux, discharge distribution.

Acknowledgements

This thesis could not have been successfully achieved without the support of professor Dr. ir. Ton Hoitink and Drs. Paul Torfs. Their inspiring lectures and expertise on River flow and Hydrology motivated myself to choose this challenging topic. I would also like to thank Msc. Karl Kästner for his valuable help and advice in numerical modeling.

I would like to extent my gratitude to all my friends from Wageningen University, especially to the members of IntegraCie (Janneke, Lysbet, Mo and Edward), who helped me to overcome cultural differences and encouraged me to explore and experience their Dutch traditions and festivities. Bedankt voor jullie hulp en vriendschap!

Finalmente quiero agradecer a Dios por todas sus bendiciones a lo largo de esta maestría, ya que sin Él no soy nada. Mi gratitud va dirigida también a mis padres, hermanos y sobrina quienes me apoyaron incondicionalmente. Gracias por sus palabras de aliento para culminar esta tesis.

Content

List of Figures

List of Tables

1 Introduction

Tidal influence on estuarine systems and single channels located beyond the limit of salt intrusion has been studied with substantial effort during the last decades [Hoitink and Jay, 2016]. Research on flow dynamics in estuarine systems becomes significant since it controls the fate and transport of sediments, contaminants, and nutrients with important consequences for deltaic deposits, landform evolution, water quality and deltaic ecosystems [Leonardi *et al.,* 2015]. In general, these studies are based on idealized systems, which mimic the interaction between river discharge and tidal waves. The idealization of river-delta landforms encompasses not only estuaries, but also bifurcations and shallow junctions located further upstream from the estuary where tidal waves might propagate or become extinct. The development of modeling environments (e.g. SLIM®, DELFT3D-FM®, FESWMS-2DH®, etc.) are useful to simulate hydrodynamical and geological processes at tidal inlets and single channels.

The aim of this thesis is to understand the mechanisms controlling the discharge division at two junction of the Kapuas River from Indonesia. This study is carried out by simulating the river discharge-tide interaction of an idealized, nonlinear model of the Kapuas River before model calibration. The hydrodynamic model was previously set up in Delft3D-FM® and will be evaluated under sensitivity analysis. Particular interest is stressed on two junctions of the Kapuas, where tidal attenuation, tidal energy and river discharge division are studied in detail.

1.1 Research background

Relevant studies about flow division at river bifurcations have been recently published. For instance, Buschman *et al.,* [2010] analyzed the subtidal flow division and water level variation on the Berau estuarine channel in Kalimantan - Indonesia. The setup of the numerical model consisted of constant river discharge at the upstream boundary, and tidally varying water level at the two sea boundaries. After performing sensitivity analysis in terms of length, width and bed roughness, the study concluded that tidal amplitude during spring and neap tides influences the tidally averaged division of river discharge.

In similar way, Sassi *et al.,* [2011] studied the tidal impact on the discharge distribution at bifurcations of the Mahakam Delta in Kalimantan, Indonesia. In contrast to the model set up mentioned above, discharge series at the upstream boundary were considered for this study. The model was forced with tides at open sea boundaries located far away from the delta. Moreover, bed roughness was conveniently segmented by discriminating fluvial parts, tidal distributaries, and the continental shelf in the model domain. This study concluded that the effect of tides is to alter the discharge division at the bifurcations that would occur without tides. The tidal impact is larger at locations closer to the sea than the ones located further upstream.

1.2 Research questions

As described in the introduction, the aim of this research is to understand the mechanisms controlling the river discharge division at the junctions of the Kapuas River. Based on that, the following research questions are proposed to reach that objective.

a. How does the tidal energy transport differ between channels connected at the junctions?

Tidal attenuation and amplification along the main river channel and the Kapuas River branches are analyzed by processing output files (model results) and computing tidal ranges at each station from the model. Tidal energy coming from the South China Sea might travel in upstream direction and reach the two junctions under study. At these locations, tidal energy may present different patterns to be analyzed (e.g. propagation, reflection, or energy balance).

b. What is the tidal influence on the discharge distribution at the junctions?

High and low river discharge in the Kapuas are simulated in order to determine the discharge division at the junctions. Analysis of the discharge asymmetry index for both high and low discharges may differ with respect to each other, and therefore, it requires to be analyzed.

2 Study area

The Kapuas is the longest river from Indonesia with a catchment size of 77000km^2 [Meybeck and Ragu, 1995], which splits into a fan shaped delta of 15km radius at the river mouth. With an annual discharge of 10000m^3/s and 1143km in length [Goltenboth *et al.,* 2006], the Kapuas River drains the major part of West Kalimantan through multiple and highly asymmetric distributaries (Figure 1). The delta is characterized by mixed tidal and riverine influence, which debouches close to the South China Sea.

Figure 1: Global view of the Kapuas River in Indonesia (A). Delta distributaries of the Kapuas (B). Place-mark icon on both maps indicates the upstream junction of this study at Soekalanting village. (Source Google maps®, 2016).

Four main river branches of the Kapuas River are illustrated in Figure 2. The junctions under study connects the Kecil branch (red line), and the Kubu branch (orange line) with the main course of the Kapuas (blue line). The junctions are located approximately at 198km and 237km from the city of Sanggau, respectively. Letters A to G indicate cross sections of interest along the Kapuas.

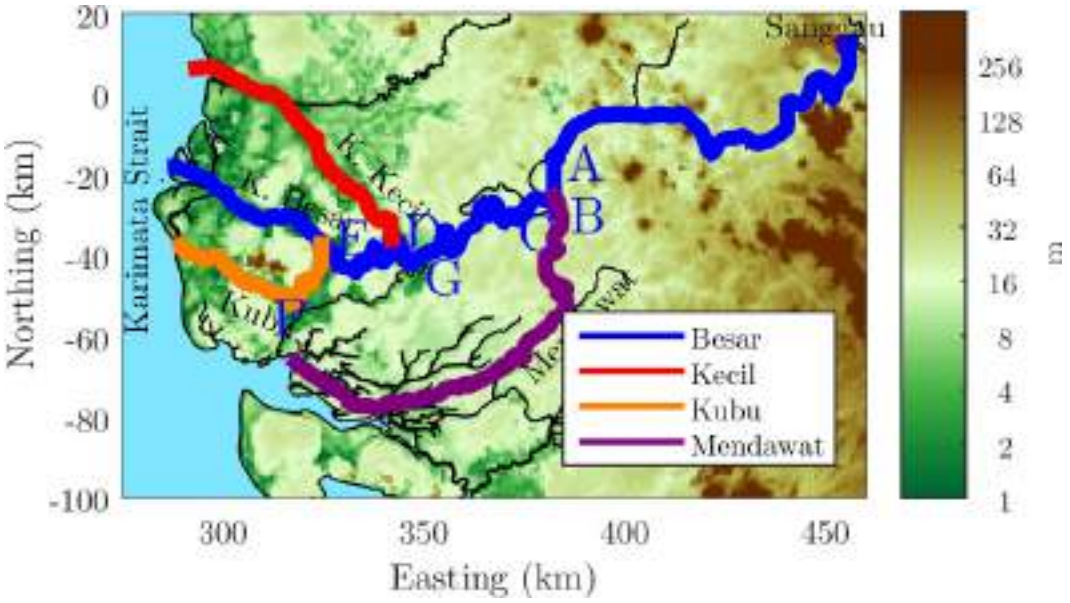

Figure 2: River branches of the Kapuas River. From top to bottom: Kecil (section D), Kapuas Besar (section E), Kubu (F) and Mendawat (section B). (Source GEBCO Digital Atlas).

Currently, hydraulic geometry and grain size trends of the distributaries are under investigation by Kästner *et al.,* [2016]. Based on field measurements, tidal regime in the Kapuas has been assorted as mainly diurnal according to the classification of Pugh [1996]. Similarly, preliminary results suggest tidal attenuation from the sea towards the distributary channels.

3 Theoretical background

3.1 Tidal characteristics

Tidal motion is generated by celestial bodies, which exert gravitational attraction on the rotating Earth. The effect of these gravitational forces are visible on the ocean when tides describe a cyclic rise and fall of the water surface. The physical explanation of tidal generation is derived from Newton's law of gravitation, which states that any particle attracts another particle with a force that depends on the products of their masses and the inverse of the square of their distance apart [Pugh and Woodworth, 2014]. Thus, not only the Sun and the Moon, but also any other celestial body can generate tides on the Earth. However, the main gravitational forces that generate tides belong to the Sun and the Moon. The magnitude of the gravitational force of the Moon is twice as large as the force of the Sun despite of the Sun's mass. As stated by Newton, the gravitational force of the Sun also depends on the square of the Sun-Earth distance, and therefore, it diminishes the gravitational force.

- Semidiurnal and diurnal tides

Tides can occur twice a day with a period of about 12 hours and 25 minutes (known as semidiurnal tide), or once a day with a period of about 24 hours (diurnal tide). Diurnal tides present one flood event (landward flow) and one ebb event (seaward flow) per day, while semidiurnal tides present two flood and two ebb events each 25 hours, approximately. Consequently, diurnal and semidiurnal tides are composed by consecutive flood-ebb events with respect to tidal currents.

The magnitude of two consecutive flood-ebb events might vary; and commonly, they are referred as a major and minor flood, and a major and minor ebb, respectively. Moreover, flood events correspond to high water *'HW'*, while ebb events correspond to low water *'LW'*, and the height difference between them is known as the tidal range. Figure 3 illustrates the tidal motion and the terms commonly used in tidal analysis.

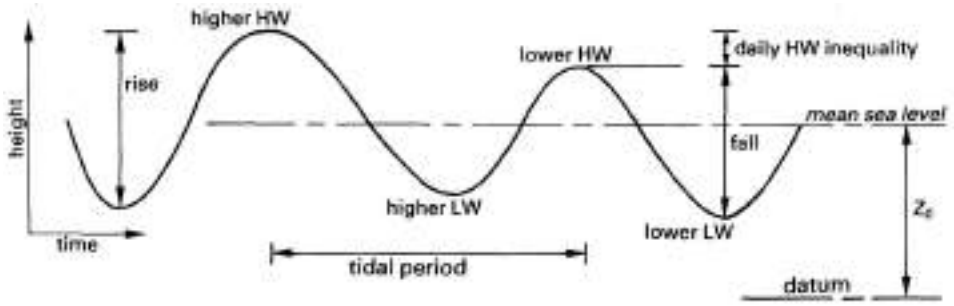

Figure 3: Schematization of tidal motion [Van Rijn, L. C., 2010].

- Spring-Neap cycle

The full relative movement of the Moon-Earth-Sun system is complex and it is responsible of tidal variability over different time scales. Apart of diurnal and semidiurnal tides, tidal range variation is noticeable during the fortnightly cycle, which elapses about two weeks. Spring and neap tides are source of fortnightly tides. Spring tides are semidiurnal tides that occur at full and new moon when the Sun and the Moon are located at the same side of the Earth or at the opposite side, respectively (Figure 4-a). This particular position leads to combination of the gravitational forces resulting in tides of increased range. Neap tides are semidiurnal tides that occur near Moon's first or last quarter when the Moon is located at 90^o respect to the Sun (Figure 4-b). However, the gravitational forces of the

Sun and the Moon are out of phase and tend to cancel each other in this position.

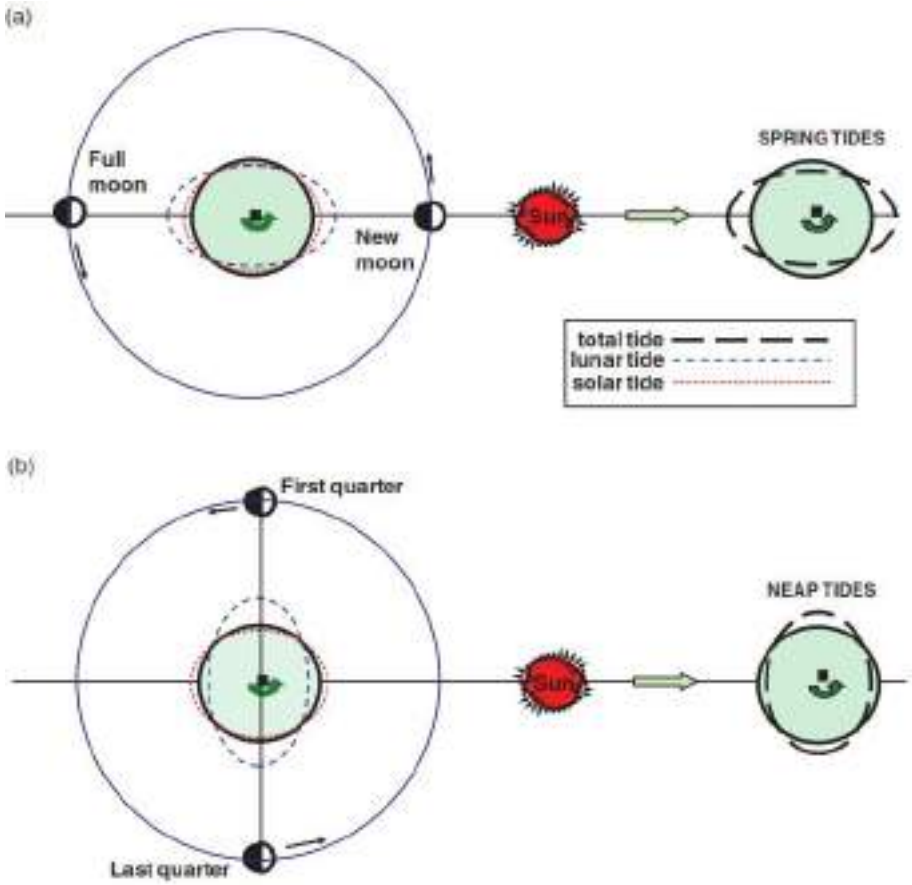

Figure 4: Relationship between the Sun and Moon phases with the spring-neap cycle. (a) Spring tides at new and full Moon. (b) Neap tides at the Moon's first and last quarter. [Pugh and Woodworth, 2014].

3.1.1 Tidal wave propagation

Water waves can be classified in long and short waves based on its wavelength to wave depth ratio. Wavelengths of roughly 10^3 to 10^4 times the wave depth are called long waves, while short waves have smaller ratios. Tidal waves are assorted as long waves due to the limited depth of the ocean and their tidal periods, which are larger than 5 minutes [Munk 1950]. Particularly, tidal waves with periods of 12 and 24 hours, are known as diurnal and semidiurnal tides.

Long waves propagate through some fixed point with a celerity (wave speed) *'c'* independently of its wave frequency *'f'*. However, they do depend on the water depth *'D'* and the acceleration of gravity *'g'* as shown in equation (1) [Pugh and Woodworth, 2014].

$$c = \sqrt{gD} \tag{1}$$

Shallow water surface waves (long waves) interact with the bottom, and as a result, the celerity slows down as the square root of the depth. It is important to mention that flow velocity *'u'* and

celerity are different concepts. The wave speed is defined as the distance traveled by a crest per unit time, whereas the flow velocity denotes the actual movement of the water. For a propagating wave, flow velocity can be expressed as function of water surface elevation *'ζ'* by the following expression [Pugh and Woodworth, 2014].

$$u = \zeta\sqrt{\frac{g}{D}} \tag{2}$$

- Phenomena affecting tidal propagation

Ocean tides are non-dispersive (i.e. the wave remains its shape as it propagates); however, as they approach towards coastal boundaries, the tidal wave is affected by wind stresses, currents, and bottom friction. Consequently, the wave shape changes and the tide becomes asymmetric. The propagation of a tidal wave in tidal channels is also affected by reflection, amplification, deformation and damping [Van Rijn, L. C., 2010].

a. Reflection

As a long wave propagates, it may encounter several obstacles on the bottom which reflects part of the energy of the incoming wave. In other words, these obstacles generate a tidal wave opposite to the incoming wave motion (Figure 5). Reflection usually occurs at coasts and estuaries, where standing waves (i.e. in the case of total reflection against a vertical boundary) or resonance effects may be experienced.

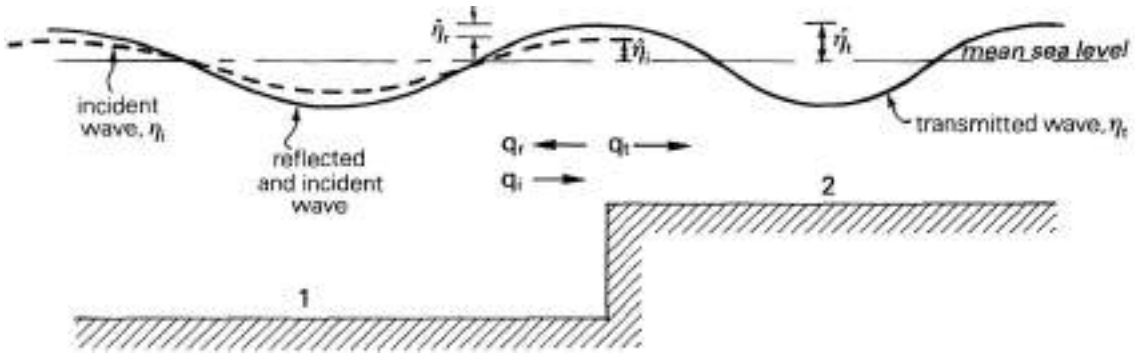

Figure 5: Reflection of tidal waves due to bottom discontinuity. [Van Rijn, L. C., 2010].

b. Amplification/Shoaling

This phenomenon takes place as a consequence of gradual changes of channel geometry (e.g. width or depth). When tidal waves propagate in convergent channels (i.e. width and depth decrease in landward direction), amplification or wave funneling occurs (Figure 6). Reduction in width of the wave front and depth increase the amplitude of the tidal wave [Pugh and Woodworth, 2014].

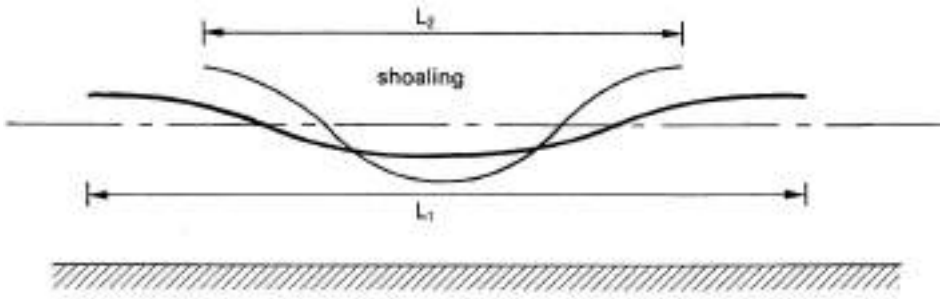

Figure 6: Amplification of tidal waves due to changes in channel width and depth in landward direction. [Van Rijn, L. C.,2010].

c. Deformation

Once tidal waves propagate into tidal channels, the transition between deep and shallow water alters the shape of the incoming wave due to non-linearity of the shallow water flow. Therefore, the sinusoidal shape of the wave changes as the wave crest travels faster than the trough, and proportionally to water level amplitude *'a_{wl}'* to water depth *'D'*. The resulting wave profile is known as wave skewness, and it is illustrated in Figure 7.

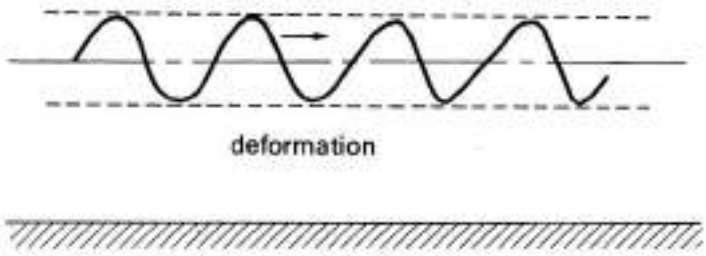

Figure 7: Deformation of tidal waves due to non-linear effects. [Van Rijn, L. C., 2010].

d. Damping

Tidal attenuation can occur as a result of friction between water flow and the bottom, which in turn leads to a loss of energy and a decrease of the wave height. Particularly, the wave height will experience an exponential decrease during propagation when the water depth remains constant along the tidal channel (Figure 8).

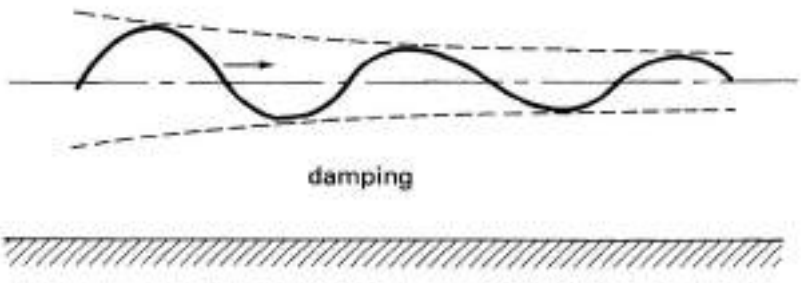

Figure 8: Damping of tidal waves due to bottom friction. [Van Rijn, L. C., 2010].

3.1.2 Tidal constituents

Six fundamental astronomical frequencies arise from the motions of the Earth-Sun and Moon-Earth system. The fundamental frequencies describe the tide-generating force based on the following parameters: solar and lunar declination, hour angle of the Sun and the Moon, and the distances Earth-Sun and Earth-Moon. Set of sinusoids based on these frequencies depicts the tide properly, especially in deep water. In shallow water (e.g. estuaries and coastal boundaries with water depths less than 200m), the tidal wave is affected by the four phenomena mentioned above. As a result, the resulting tidal wave generates constituents whose frequencies differ from the main tidal constituents. Table 1 presents the periods, frequencies and relative coefficients of the seven major astronomical constituents. These coefficients indicate their relative contribution to the total tidal amplitude of the Equilibrium Tide.

Table 1: Principal tidal constituents [Defant 1961].

Constituent	Origin	Period (T) [h]	Frequency (f) [1/h]	Relative coefficient (M_2)
M_2	Principal lunar	12.42	0.081	1.00
S_2	Principal solar	12.00	0.083	0.47
N_2	Larger lunar elliptic	12.66	0.079	0.19
K_2	Luni-solar semidiurnal	11.97	0.084	0.13
K_1	Luni-solar diurnal	23.93	0.042	0.58
O_1	Principal lunar diurnal	25.82	0.039	0.42
P_1	Principal solar diurnal	24.07	0.042	0.19

3.2 Tides in rivers

In alluvial estuaries, tides meet the river stream and propagate in upstream direction. However, as the tides progress, they are dissipated by bottom friction and riverine flow. Leonardi *et al.,* [2015] showed that the presence of river discharge has the same effect as increasing friction by a factor proportional to the riverine to the tidal discharge ratio. Therefore, the loss of energy (dissipation) along the river leads to highly non-linear physical process [Pugh and Woodworth, 2014].

The shape of alluvial estuaries is similar all over the world Van Rijn, L. C., [2010]. Generally, these estuarine systems are characterized by narrow and shallow regions connecting the estuary with tidal channels. Gradual narrowing of the tidal channels in landward direction implies reduction of their cross-section area, which results in converging channel system, also known as funneling. Consequently, tidal amplitudes tend to increase in the channel system as the tides propagate in upstream direction.

3.2.1 Standing and progressive waves in shallow water

Tidal propagation in the oceans is not affected by amplification, damping or reflection even though atmospheric forcing mechanisms can exert a drag force on the water surface and alter the tidal waves. The relative large depth of the oceans and the negligible bottom friction do not alter tidal progressive waves. In contrast to oceans, shallow water waves experience bottom friction due to the relative small channel depths. In addition, shallow channels may exhibit properties of both standing and progressive waves [Buschman *et al.,* 2010].

Progressive waves propagate with a phase speed of approximately $\sqrt{gD}$, and the tidal range remains

constant along the channel provided that the effects of friction balance the effects of width convergence [Buschman *et al.,* 2010]. Furthermore, as the tide propagates in upstream direction, the shape of the tidal wave may be distorted by the generation of super harmonics. For a tidal wave, the phase delay between water level and velocity is defined as the phase lag between high water (high tide) *'HW'* and high water slack *'HWS'*.

The phase lag of flow velocity with respect to water surface level tends to 0^o for progressive waves. Therefore, ebb and flood occur at high and low tide, respectively. Standing waves on the other hand, occur when the phase difference between flow velocity and water surface level tends to 90^o. Likewise, slack periods (i.e. when the flow velocity is zero) occur at high and low tide as can be seen in Figure 9.

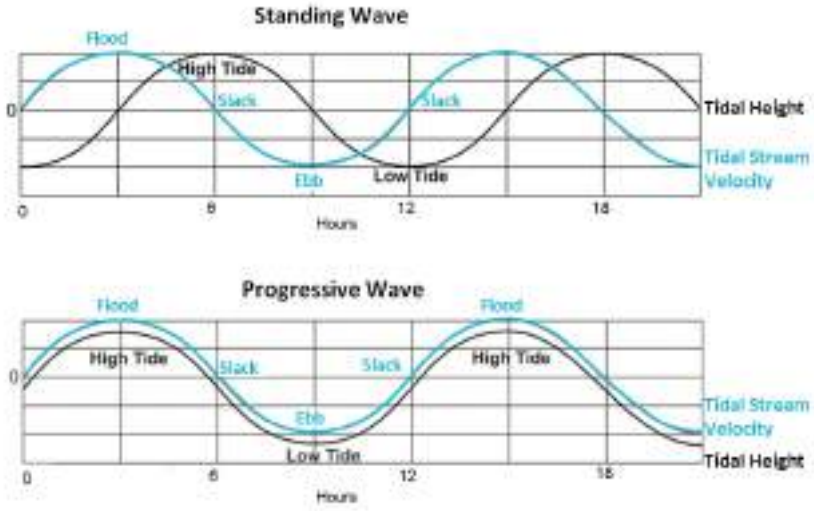

Figure 9: Standing and progressive waves. [Tidal Current Predictions and Data - NOAA].

3.2.2 Tidal energy transport

The dynamics of the Moon-Earth-Sun system constitute the astronomical forcing of the oceans, and thus, the source of energy. The tidal energy is propagated from the major ocean basins to shallow shelf regions by progressive waves. In these regions, the tidal energy is dissipated and transformed into turbulence due to bottom friction effects. At tidal rivers however, tides propagates until becoming extinct by bottom friction effects and riverine flow in the upstream part of the river.

The tidal energy transport for diurnal and semidiurnal tides can be calculated by applying the equation of Gill, [1982].

$$\overrightarrow{F} = \frac{\rho g H}{T} \int_0^T \zeta \overrightarrow{u} \, \mathrm{d}t \tag{3}$$

Where, *'$\overrightarrow{F}$'* represents the vertically integrated barotropic energy flux in [W/m], *'ρ'* is the water density, *'g'* is the gravitational acceleration, *'H'* is the water depth, *'T'* is the tidal period, *'ζ'* is the surface elevation, and *'$\overrightarrow{u}$'* is the flow velocity.

4 Methods

4.1 Methodology

According to the research questions, three main phenomena will be studied in the Kapuas River: tidal attenuation, tidal energy transport and discharge distribution. A 2D-model approach will be adapted in DELFT3D-FM® in order to simulate river discharge-tide interaction and to address the proposed research questions.

Tidal attenuation from output results will be calculated and compared with previously results based on field measurements. Tidal energy, associated with progressive waves from the tidal motion in the downstream channels of the Kecil and Kubu junctions, will be also studied in detail. Ultimately, flow division on the junctions will be investigated as river discharge might be tidally influenced from the Kecil and Kubu delta distributaries, respectively. In addition, for both tidal attenuation and flow division, sensitivity analysis is proposed. Sensitivity analysis in terms of tidal attenuation and flow division may also reveal contribution of the individual model parameters (e.g. river discharge, bed roughness and mean bed level). Additional parameters, such as bed slope and channel depth are not part of the sensitivity analysis since they are fixed to the bathymetry of the Kapuas River. Consequently, any change in bed slope or channel depth implies an adjustment of the current bathymetry, and for matter of time, it is considered out of the scope of this study.

The time frame (model run period) is divided in two sections, which correspond to the sensitivity analysis with fifty scenarios, and the simulation of two scenarios. The model runs for high and low river discharges were set to five months, from December - 2014 to April, - 2015, and to one month (November-2014) for sensitivity analysis. After each simulation, the output results are processed in MATLAB® scripts.

For tidal analysis two approaches are developed: wavelet analysis and harmonic analysis. The first approach enables to get diurnal D_1 and semidiurnal species D_2, whereas the second one is used to determine individual tidal constituents: diurnal (O_1, P_1 *and* K_1) and semidiurnal (M_2 *and* S_2). Those constituents are chosen following the Tide-tables of the Kapuas as indicated in the respective section. Calculation of tidal attenuation is based on the first approach, while computation of tidal energy is carried out with harmonic analysis. Nevertheless, both tidal attenuation and tidal energy can be computed with the two approaches, indistinctly. The selection of each approach is a matter of convenience for further analysis. The scripts for those approaches are available in MATLAB®. Only sensitivity analysis is performed in RStudio® by using Drs. Paul Torfs' scripts, which were provided during the course "Water and Air flow Numerical Techniques".

4.2 Analysis of variance

Analysis of variance *'ANOVA'*, developed by Ronald Fisher in 1918, is a statistical method commonly used to compare the differences of means between two or more groups of data. This method states that the variance of a variable (e.g. model result) can be decomposed or partitioned into contributions from each source of variation (e.g. model parameters). *ANOVA* is based on three assumptions.

a. Independence: model parameters are independent from each other.

b. Normality: model residuals have a normal (Gaussian) distribution.

c. Homogeneity or equality: all groups of model parameters have the same or similar variance.

The following example is proposed for explanation. Let us consider maximum river discharges as model result *'M'* from several simulations in a hydrodynamic model. Besides, the model parameters involved in such simulations are defined as follows: incoming upstream flow *'p_1'*, bed roughness *'p_2'*, bed slope *'p_3'*, and bed level *'p_4'*. All of them represent sources of variation to the model result, and they are independent from each other. After applying ANOVA to this model setup, the variance of M can be partitioned into both individual and group contributions of p_1, p_2, p_3 and p_4.

4.2.1 Latin hypercube sampling

Latin hypercube sampling *'LHS'* is a technique used to create parameter samples. This sampling technique has become widely used for the propagation of uncertainty in analyses of complex systems. The usefulness of *LHS* is based on the ability to produce stable results (i.e. less variation in estimated distribution functions from sample to sample) [Helton and Davids, 2003], which clearly improve random sampling techniques such as the Monte Carlo approach.

- Advantages of LHS over Monte Carlo

In Monte Carlo analysis, the procedure to generate the parameter sample is less sophisticated than *LHS*. In Monte Carlo approach there is no assurance that a sample element will be generated from any particular subset of the parameter sample. Therefore, this sample will lead to non-stable histograms, undesirable clustering of points, and unsampled spaces as illustrated in Figure 10.

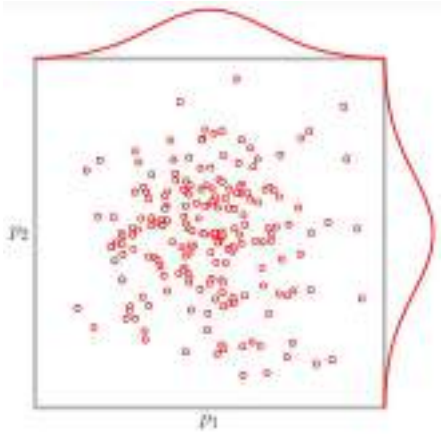

Figure 10: Monte Carlo approach in two dimensions (p_1 and p_2). Red empty points show sample values from p_1 and p_2. Red lines indicate normal distribution of each parameter. (Source: Paul Torfs' lecture notes).

On the other hand, *LHS* generates controlled random samples since its basis arises from the quantile sampling. Therefore, the sampling distribution is close to the probability density function. In other words, each element of the sample is generated by splitting the range of the subset parameter in parts with equal probability as shown in Figure 11.

Thus, each parameter sample has its unique base value (mean) and its own scale of variation (standard deviation). Consequently, histograms of the samples are more stable and are able to determine true probability densities. Furthermore, the contribution to the variance of the model result can easily be determined by means of its conditional expectation (i.e. prediction of the model result as function of its parameters) as shown in Figure 12.

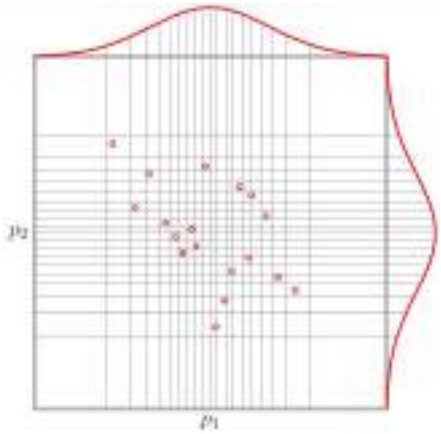

Figure 11: Latin hypercube sampling in two dimensions (p_1 and p_2). Red empty points show sample values from p_1 and p_2. Red lines indicate normal distribution of each parameter. (Source: Paul Torfs' lecture notes).

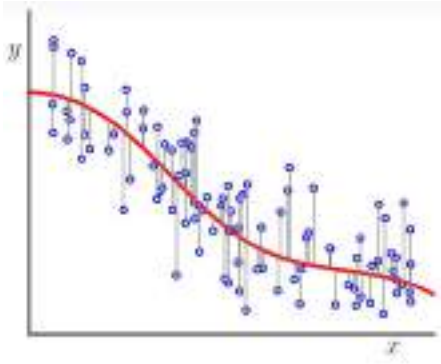

Figure 12: Conditional expectation of y given x (x->E[Y|X=x]). (Source: Paul Torfs' lecture notes).

4.3 Harmonic analysis

Tidal variation can be represented as the sum of N-finite and stationary harmonic terms (i.e. set of sinusoids) at specific frequencies *f*. This assumption neglects non-linear effects derived from non-astronomical forcing functions (e.g. wind effects, river discharge, etc.). Yet, it is the basis of harmonic analysis. The harmonic terms are written in the form:

$$\eta = a_N cos(\omega_N T - g_N) \tag{4}$$

where, η is the water level, *'a_N'* is the amplitude in [m], *'ω_N'* is the angular velocity specified by the combination of six fundamental frequencies [rad/s], and *'g_N'* is the phase lag of the equilibrium tide relative to the Greenwich meridian [rad].

4.4 Wavelet analysis

In contrast to harmonic analysis, wavelet analysis addresses non-stationary processes occurring over finite and temporal domains. The wavelet transform *'WT'* examines time series whose non-stationary power occurs at many different frequencies [Torrence and Compo, 1998]. Based on generalized local base functions (wavelets), WT scales and translates the wavelets in both frequency and time domain, also known as the wavelet domain *'WD'*. The highest frequencies of a signal are resolved by narrowing the *WD*, whereas the lowest frequencies are reached by widening the *WD* However, this flexible resolution in frequency *'ω'* and time *'t'* is not arbitrary and does depend on each other. In other words, any increase in the frequency resolution implies low precision in time localization in the high frequency band, and vice versa for low frequency components [Lau and Weng, 1995]. Figure 13 illustrates the relationships between frequency, time and space in WT.

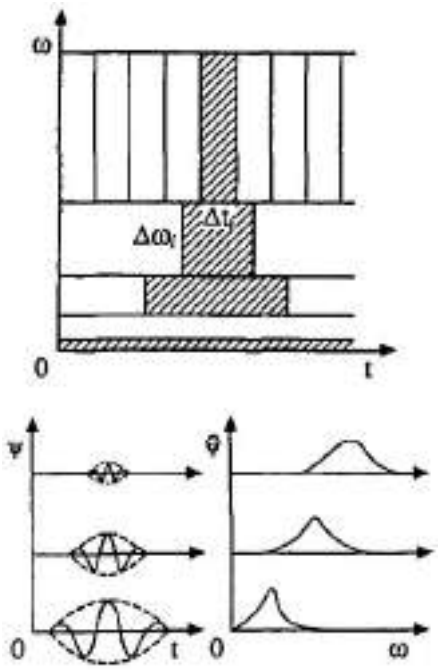

Figure 13: Time-frequency window used in wavelet transform WT and their correspondent time series represented in time space and frequency space. [Lau and Weng, 1995].

Hence, a signal can be decomposed by WT in terms of some elementary functions derived from a mother wavelet *'$\psi(t)$'*, and redefined as a convolution integral of ψ. Furthermore, the signal can be formally reconstructed from the wavelet coefficients by an inversion formula. For further mathematical derivation, see Lau & Weng [1995] and Torrence & Compo [1998].

4.5 Delft3D flow flexible mesh (DELFT3D-FM®)

DELFT3D-FM® is a hydrodynamical simulation program developed by Deltares, in 2015. This software combines unstructured and structured modeling of water related flows. This modeling approach allows numerical simulations for coastal, river and estuarine areas. The numerical concept is based on the combination of both 2D and 3D finite volume cells with 1D-flow networks.

The advantage of this novel approach lies on its accuracy and efficiency when considering hybrid networks (i.e. curvilinear grids and the possibility of local refinement of the mesh). Therefore, re-

strictions and poor grid resolution imposed by traditional structured grids; specifically at the grid boundaries, are overcome by means of grid coupling via triangles, quadrilaterals and pentagons. Figure 14 illustrates the so called hybrid networks.

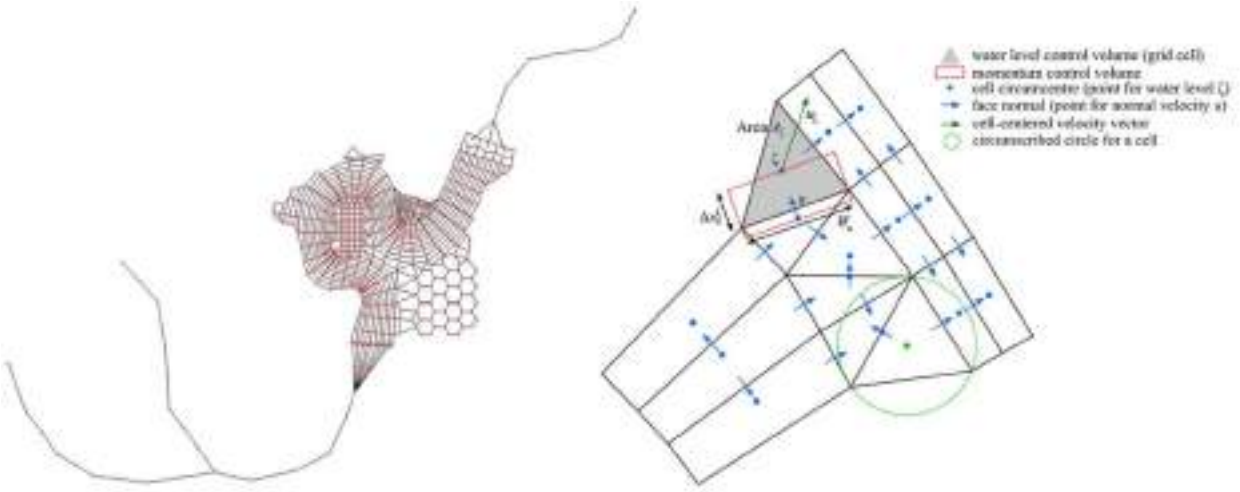

Figure 14: Conceptual models of unstructured grids: coupling 1D river with 2D grid (left), and triangles and quadrangles (right). [Kernkamp et al., 2011].

4.5.1 Hydrodynamics

Shallow water equations for 2D (depth-averaged) modeling and 3D (σ- and z-layers) are solved by DELFT3D-FM®. These equations are derived from the three dimensional Navier-Stokes equations for incompressible free surface flow, and under the Boussinesq assumptions. The set of partial differential equations in combination with an appropriate set of initial and boundary conditions are solved on an unstructured finite volume grid [D-FlowFM user's manual, 2017]. The 2D modeling approach solves the Saint-Venant equations that are considered in this study. The equations of conservation of mass and momentum balance for the 2D-approach are expressed as follows.

$$\frac{\partial \overrightarrow{\zeta}}{\partial \overrightarrow{t}} + \nabla\left[(h+\zeta)\overrightarrow{u}\right] = q \tag{5}$$

The continuity equation is solved implicitly for all points in a single combined system [D-FlowFM user's manual, 2017].

$$\frac{\partial \overrightarrow{u}}{\partial \overrightarrow{t}} + \overrightarrow{u}\nabla\overrightarrow{u} + \frac{1}{\rho_o}\nabla P + \frac{c_f}{h+\zeta}|\overrightarrow{u}|\overrightarrow{u} = \upsilon\nabla^2\overrightarrow{u} + \overrightarrow{F} + \overrightarrow{M} \tag{6}$$

On the other hand time integration is done explicitly for part of the advection term [D-FlowFM user's manual, 2017]. The explicit scheme is limited by the Courant criterion (i.e. the numerical domain of dependence must contain the mathematical domain to avoid incorrect results in the simulation) with respect to the time-step.

Where,

$\overrightarrow{u} = \mathrm{u}_x \overrightarrow{i} + \mathrm{u}_y \overrightarrow{j}$: depth-averaged velocity vector,

h: water depth (respect to level z=0),

ζ: surface elevation (respect to a base level z=0),

c_f: bed friction coefficient ($\mathrm{c}_f = \frac{g}{C^2}$),

C: Chézy friction coefficient,

υ: kinematic viscosity,

g: gravitational acceleration,

$\overrightarrow{F} = \mathrm{F}_x \overrightarrow{i} + \mathrm{F}_y \overrightarrow{j}$: represents the unbalance of horizontal Reynolds stresses,

q: contribution per unit area due to discharge or withdrawal of water, precipitation and evaporation.

$$q = \int_0^h (\mathrm{q_{in}} - \mathrm{q_{out}})\,\mathrm{d}z + P - E \tag{7}$$

$\overrightarrow{M} = \mathrm{M}_x \overrightarrow{i} + \mathrm{M}_y \overrightarrow{j}$: external forcing term. Contributions of external sources or sinks of momentum (external forces by hydraulic structures, discharge or withdrawal of water, wave stresses, etc.).

5 Available field measurements

The data required for this research was collected during field campaigns from October 2013 to May 2015. Therefore, data collection is not considered part of this thesis. A briefly summary of the data used in this study is indicated below.

5.1 Bathymetry

A bathymetric survey was carried out from the South China Sea to Sanggau by using a simple beam echo sounder. The data was interpolated with survey measurements in the Kapuas River and available data from the sea [General Bathymetry Chart of the Oceans - GEBCO]. Figures 15 and 16 show the bathymetry of the junctions under study.

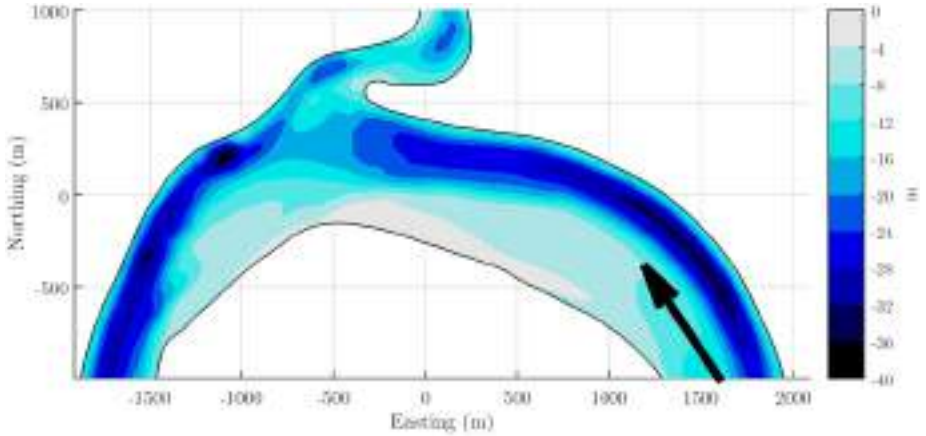

Figure 15: Bed level of the first junction, which debouches into the Kecil distributaries. Black arrow indicates flow direction towards the junction.

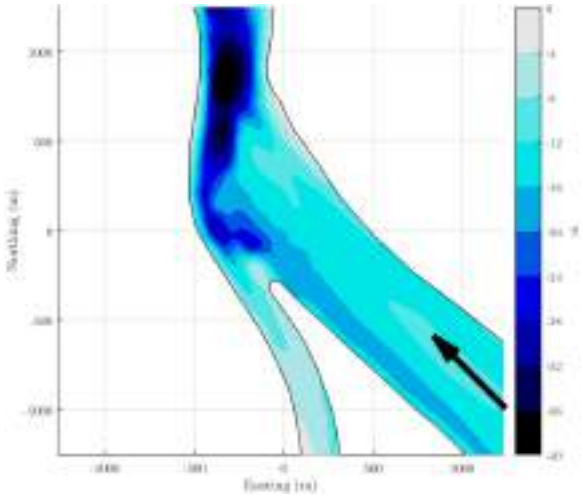

Figure 16: Bed level of the second junction, which debouches into the Kubu distributaries. Black arrow indicates flow direction towards the junction.

5.2 River discharge

Discharge records at the Sanggau station were collected during field campaigns. Figure 17 illustrates time series of the Kapuas discharge. Perpendicular lines indicate the time frame for sensitivity analysis and simulation of high and low discharges, which will be described later on.

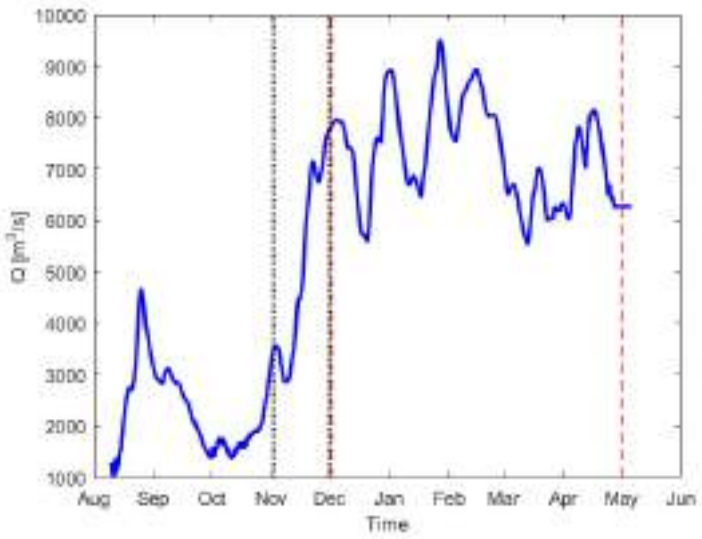

Figure 17: River discharges at Sanggau station. Black dotted lines indicate time frame for sensitivity analysis. Red dashed lines indicate time frame for model run.

5.3 Sea water level

Sea water level from the South China Sea was obtained from the global model of ocean tides *'TPXO'* on a 1440x721, 1/4 degree resolution full global grid. *TPXO* describes tides as complex amplitudes of earth-relative sea-surface elevation for eight primary (M_2, S_2, N_2, K_2, K_1, O_1, P_1, Q_1), two long period (M_f, M_m) and three non-linear (M_4, MS_4, MN_4) harmonic constituents. Further information of *TPXO* can be found at (http://volkov.oce.orst.edu/tides/global.html). The tide forcing at the sea is presented in Figure 18.

5.4 Tide tables

Selection of basic astronomic constituents for the Equilibrium Tide is sometimes difficult and requires certain level of expertise. However, as stated by Pugh and Woodworth [2014], there are some basic rules that can be followed (e.g. Rayleigh criterion, see section 7.1.1). Fortunately, tide tables based on tidal records and regional knowledge of the Indonesian Archipelago have been published before this study and are available for tidal analysis. Table 2 presents the main constituents of the Kapuas-Kecil branch.

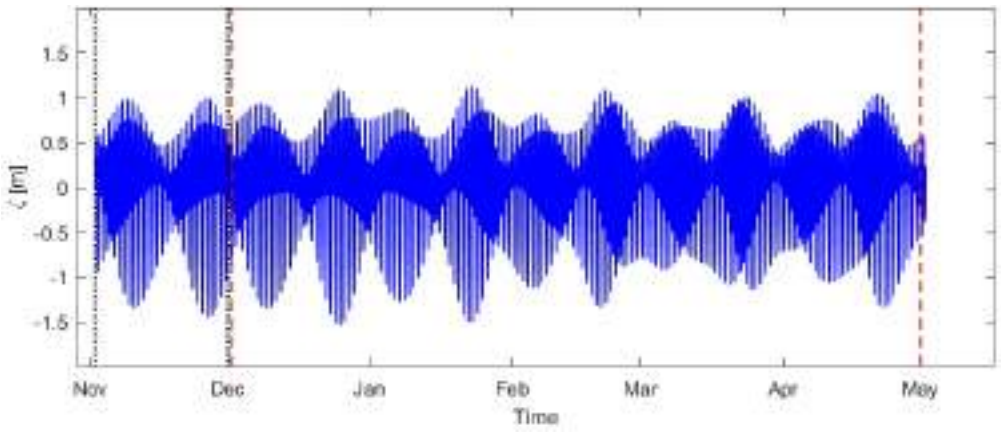

Figure 18: Surface water level at the South China Sea extracted from TPXO. Black dotted lines indicate the time frame for sensitivity analysis. Red dashed lines indicate the time frame for model run.

Table 2: Tide table of the basic astronomic constituents for the Kapuas River. [Tide tables. Indonesian archipelago, 2003].

Latitude: $00^o.1$ S										
Longitude: $109^o.1$ E				**Sungai Kapuas Kecil**						
Time: G.M.T. +07.00										
Predictions are referred to Chart Datum 9 dms below MSL										
Tidal constants:	**M_2**	**S_2**	**N_2**	**K2**	**K_1**	**O_1**	**P_1**	**M_4**	**MS_4**	**Z_0**
Amplitude in cm:	16	9	-	-	39	32	10	-	-	90
360^o - g^o	232	210	-	-	235	304	234	-	-	-

5.4.1 Lunar phases

Information of the lunar phases at Pontianak (Figure 1) is presented in Table 3 (source: www.timeanddate.com/moon/phases/indonesia/pontianak).

Table 3: Lunar phases at Pontianak - Indonesia.

Year	New Moon		First Quarter		Full Moon		Third Quarter		Duration
2014	22-Nov	19:32	29-Nov	17:06	6-Dec	19:26	14-Dec	19:50	29d 13h 04m
	22-Dec	08:35	29-Dec	01:31					29d 11h 38m
2015					5-Jan	11:53	13-Jan	16:46	29d 11h 38m
	20-Jan	20:13	27-Jan	11:48	4-Feb	06:08	12-Feb	10:49	29d 10h 34m
	19-Feb	06:47	26-Feb	00:14	6-Mar	01:05	14-Mar	00:47	29d 9h 49m
	20-Mar	16:36	27-Mar	14:42	4-Apr	19:05	12-Apr	10:44	29d 9h 21m
	19-Apr	01:56	26-Apr	06:55	4-May	10:42	11-May	17:36	29d 9h 16m

6 Model setup

6.1 Mesh

- Domain extent

The extent of the mesh was previously determined before the development of this study. The mesh encompasses large part of the Kapuas River, which flows from the Northeast part of West Kalimantan (at Sanggau) to the Southwest part and debouches at the sea. Likewise, the mesh covers a significant part of the South China Sea by following a semi-hexagonal pattern at the edge as shown in Figure 19 (blue line). Moreover, Figure 19 shows how the boundary conditions are placed at locations quite far from the junctions under study (red box). In this way, any numerical disturbance due to boundary conditions is avoided when running the model.

Figure 19: Domain extent and boundary conditions of the Delft3D-FM® numerical model. Red box below Pontianak outlines the junctions of interest. Blue polyline shows the semi-hexagonal edge at the sea. Green points at the corners of the polyline indicate locations of the downstream B.C. Cyan diamond at Sanggau indicates the location of the upstream B.C.

- Boundary conditions

The tidal and riverine information presented above were assigned to the open boundaries at the seaward and landward parts of the model, respectively. A prescribed gradient (i.e. river discharge) was imposed at the upstream part of the Kapuas River (Figure 19 - cyan diamond). Therefore, Dirichlet boundary conditions at Sanggau were set for different discharges depending on the aim of the model run (i.e. sensitivity analysis or simulation of high and low discharges). The semi-hexagonal edge at the South China Sea was previously configured in order to improve the interpolation of Dirichlet boundary conditions (i.e. fixed state of sea water levels). DELFT3D - FM® captures boundary conditions

through endpoints of a line imposed by the user (green points), and thus, a polyline resembling the hexagonal shape of the edge at the Sea may improve the interpolation.

6.2 Input model parameters

As mentioned in above, the mesh, model domain and boundary conditions were already configured before the start of this study. Nevertheless, the model set-up consisted in determining the input model parameters, time step and time frame in DELFT3D-FM®. Those values were set up separately for sensitivity analysis and for simulation of two scenarios: high and low discharges in the Kapuas River. In addition, observation points and cross sections were placed along the Kapuas River in order to get the model results.

The parameters considered for the model runs are summarized in Table 4.

Table 4: Input model parameters for Delft3D-FM® model.

Description	Parameter	Unit	Value
Maximum Courant Number	CFL_{max}	-	0.7
Eddy viscosity	υ	$[m^2/s]$	1
Chézy coefficient	C	$[m^{1/2}/s]$	70
Bed slope	s	[m/m]	1.2 E-4

Other parameters, mainly related to sediment transport analysis, were not taken into account un this study, and consequently, they were set up as default values.

6.3 Time step

The quality of approximation and convergence of the model depends on the time step and the numerical scheme used for solving the Saint-Venant equations, respectively. As a rule of thumb, the smaller the time step the better the numerical solution. Therefore, the set up of the time step should be small enough to reach convergence, avoid possible instabilities, and more importantly, it should keep numerical quality. Unfortunately, as the time step approaches to zero, the computation time/cost increases and the model run can take several days.

The time step for modeling both sensitivity analysis and the two scenarios was set to five minutes. Similarly, the output parameters (e.g. water levels, flow velocities, cross section areas and discharges) are available in history (his) files (i.e. time series data based on observation points, cross sections and structures) and reproduced with a time interval of five minutes too. It is also possible to retrieve flow quantities of the entire grid at specified time intervals through map files. However, the map files require complex scripts encoded in MATLAB® to extract the output parameters. As a result, only his files were used for further calculations.

6.4 Observation points and cross sections

Observation points and cross sections (polylines) in DELFT3D-FM® are required to register time series data of the output parameters. The data retrieved from observation points account for water levels, water depths and velocities (point) recorded in time at the closest node from the grid. Cross sections on the other hand, reproduce channel areas, discharges and velocities in time. It is worth to

note that cross section velocities are computed as the ratio of discharge over area, and therefore, they do differ with respect to velocity points. The methodology and conventions considered for setting the observation points and cross sections down along the Kapuas River are described below.

The cross sections are placed in such way that the flow is assumed positive in offshore direction, while negative values indicate reverse flow in landward direction. To identify the cross sections, the name of the closest location to the Kapuas River is included as reference. Moreover, numeration of the cross sections follows the seaward direction (from upstream to downstream part of the river). At the bifurcation, the river branch is numbered before continuing with the numeration of the main channel as indicated in Figure 20.

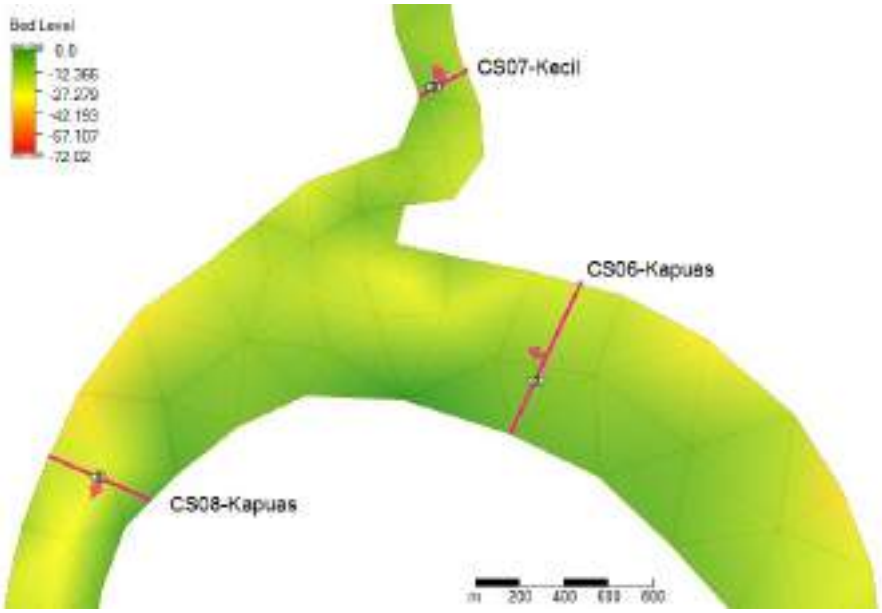

Figure 20: Cross sections (pink line) and observation points (eye-icon) at the Kecil-Kapuas junction. Arrows indicate positive flow direction. Labeling corresponds to the cross sections.

Observation points are numbered following the same methodology applied for cross sections, but this time with different notation. First, the location of the available gauge stations are considered as observation points, and intuitively, they are named according to the water level map gauge (see Figure 37 in the Annex). Nevertheless, additional observation points are required to perform tidal analysis, especially at the junctions. For that reason, new observation points are added and numbered on the Kapuas Rivers as shown in Figure 21.

6.5 Setup of sensitivity analysis

Sensitivity analysis of the model results is based on fifty scenarios. The scenarios contemplate an interplay of principal features of the Kapuas River, such as river discharge, tidal forcing, bed roughness and bathymetry. The time frame for such analysis is conveniently set from one month (November, 2014), in which the river discharge increases rapidly passing from low flow ($\sim$3000m^3/s) to high flow ($\sim$8000m^3/s) as indicated in Figure 17. In that way, the sensitivity analysis captures the maximum and minimum discharges measured in the Kapuas, and it resembles the corresponding tidal forcing during the same period. However, the model runs are based on constant river discharges during the entire month of simulation. Besides, the length of the model run period encompasses the spring-neap cycle for further analysis.

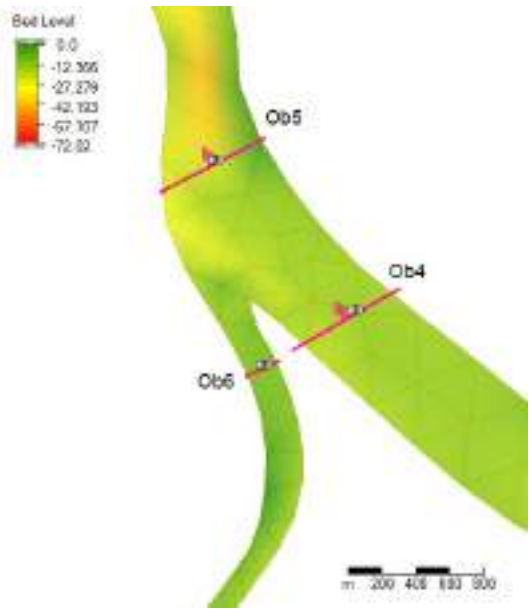

Figure 21: Cross sections (pink line) and observation points (eye-icon) at the Kubu-Kapuas junction. Arrows indicate positive flow direction. Labeling corresponds to observation points.

The analysis of variance *'AVS'* technique, based on a Latin Hypercube sampling, is applied to construct the parameter sample as described in section 4.2. The model parameters considered for the sensitivity analysis are bed roughness, river input discharge and mean bed level

- River discharge

High and low flow thresholds are required to define the range of river discharge in the Kapuas. Based on Figure 17, maximum discharges reach values of about 9500m^3/s, while minimum discharges are close to 1000m^3/s. Thus, the mean river discharge is 5150m^3/s approximately. Likewise, the standard deviation is calculated for the entire discharge records (October/2013 to May/2015) giving a value of roughly 2357 m^3/s. Besides, it is worth to mention that the mean river discharge from all records is quite similar to the mean discharge of November/2014.

- Bed roughness

Former studies in the Kapuas estuary [Deynoot, 2011], defined a Chézy coefficient of 60m$^{1/2}$/s for the downstream part of the Kapuas Kecil branch and a value of 30m$^{1/2}$/s for the meandering part of the river (Figure 38 in the Annex). Those values are averaged out giving a base value of 45m$^{1/2}$/s. This value is considered suitable since common bed roughness values are about 55 m$^{1/2}$/s for tidal channels [Buschman *et al.,* 2010]. The scale of variation was imposed to 15 m$^{1/2}$/s, which encompasses conservative bed roughness values suggested in literature [Te Chow, 1959].

- Mean bed level

Bed slope and channel depth are not considered for sensitivity analysis. These two model parameters are part of the bathymetry, and instead of them, it is proposed to investigate the contribution of the mean bed level variation to the model result. Hence, fifty tentative bathymetries for the Kapuas River

are created and coupled to the mesh. The initial mean bed level is considered as the base value, while a standard deviation of 1.50m respect to the initial bed level is set for further analysis.

Table 5 summaries the base values and scales of variation for the model parameters.

Table 5: Base values and scale of variation used to create the parameter sample according to the Latin Hypercube Sampling technique.

Model parameter	Symbol	Unit	Base value	Scale of variation
Bed roughness	C	$[m^{1/2}/s]$	45	15
Mean bed level	d	[m]	0	1.50
River discharge	Q_{in}	$[m^3/s]$	5150	2357

Table 12 and 13 in the Annex contains the model input values for the fifty model runs and basic statistics derived from the parameter values, respectively. Likewise, the sampling distribution and the histograms based on the parameter values are shown in Figures 42 and 43 in the Annex.

7 Simulation results

7.1 Tidal analysis

After the simulations, the time series of water levels and velocities were decomposed in diurnal and semidiurnal species through harmonic and wavelet analysis.

7.1.1 Harmonic analysis

The script *'T-tide'*, developed by Pawlowicz *et al.,* [2002], allows reconstruction of water level and velocity records based on harmonic analysis. According to the Tide-tables of the Kapuas (see section 7.1.6), the reconstruction can be restricted to the five main tidal constituents (O_1, P_1, K_1, M_2 and S_2). This can be done by editing T-tide in MATLAB® and setting the Rayleigh resolution up to these five constituents.

- Rayleigh criterion

This criterion states: *"Only constituents that are separated by at least a complete period from their neighboring constituents over the length of data available should be included in tidal analysis"* [Pugh and Woodwordth, 2014]. Therefore, the model results should be large enough to comply with this criterion. As example, the calculation of the Rayleigh criterion for P_1 and K_1 is presented below.

$$360^o \;/\; \left[\; (15.04\ [^o/\text{hour}] - 14.96\ [^o/\text{hour}]) \times 24\ [\text{hour/day}] \;\right] = 182.48\ [\text{day}]$$

Table 6 shows the Rayleigh criterion for the tidal constituents based on their angular speeds.

Table 6: Rayleigh criterion calculated for the five main tidal constituents in the Kapuas River. Adapted from [Pugh and Woodworth, 2014].

Constituent	Angular speed (ω) [^{o}/hour]	Origin	Rayleigh Criterion [day]
O_1	13.94	Principal lunar diurnal	
	14.49	Smaller elliptical lunar	
			14.77
			31.81
P_1	14.96	Principal solar diurnal	
			182.48 (∼6 months)
K_1	15.04	Luni-solar diurnal	
M_2	28.98	Principal lunar	
			14.77
S_2	30.00	Principal solar	

From Table 6, it can be followed that roughly six months are needed to distinguish both luni-solar diurnal and principal solar diurnal constituents from the Kapuas River. Unfortunately, the model run encompasses a time frame of five months due to computation time limitations. Although one month is missing to comply with the Rayleigh criterion, the harmonic analysis is yet considered valid.

The amplitudes and phases of the tidal constituents at the junctions are shown in Table 7 and 8. The tables clearly show that the larger diurnal and semidiurnal amplitudes belong to K_1 and M_2 , respectively. High river discharge corresponds to small tidal amplitudes, while higher amplitudes are experienced during low river discharge at the junctions.

Table 7: Overview of the five main tidal constituents obtained from harmonic analysis for high and low flow at the Kecil-Kapuas junction.

Constituent	High flow (10000m^3/s)		Low flow (1000m^3/s)	
	Amplitude [cm]	Phase [^{o}]	Amplitude [cm]	Phase [^{o}]
K_1	8.22	178.60	16.04	164.67
O_1	6.32	104.00	11.98	96.49
P_1	2.97	173.20	5.60	160.31
M_2	6.03	213.94	20.36	172.42
S_2	2.14	274.35	6.97	238.02

Table 8: Overview of the five main tidal constituents obtained from harmonic analysis for high and low flow at the Kubu-Kapuas junction.

Constituent	High flow (10000m^3/s)		Low flow (1000m^3/s)	
	Amplitude [cm]	Phase [^{o}]	Amplitude [cm]	Phase [^{o}]
K_1	12.67	160.20	20.29	144.33
O_1	9.65	87.24	14.69	76.56
P_1	4.55	155.13	7.14	141.52
M_2	9.36	181.80	23.87	152.78
S_2	3.27	242.28	8.00	216.89

7.1.2 Wavelet analysis

Similarly, water level and velocity records derived from the gauge stations of the Kapuas and the observation points were processed through wavelet transform. The mean tidal amplitude for diurnal *'D_1'* and semidiurnal *'D_2'* species as well as the tidal range at the gauge stations are presented in Table 9. Additionally, the same information for the two river branches can be found in Tables 10 and 11 in the Annex.

The same remarks, as compared to harmonic analysis, can be noticed in Table 9. Low river discharge leads to larger tidal amplitudes at D_1 and D_2 than the ones computed during high river discharge. Moreover, gauge stations located close to the sea experience higher tides than the other stations. Diurnal tidal amplitudes are in general larger than the semidiurnal for both high and low river flow. However, the semidiurnal tides are slightly higher than the diurnal tides at Terentag and Teluk Bajur stations. These stations are close to the Kecil-Kapuas junction as indicated in Figure 37 in the Annex. The latter occurs only during low river discharge.

Figure 22 shows the tidal amplitudes at the junctions for high and low river flow. From December to the middle of February, the amplitudes of the tidal species are in phase, but in the following months, the diurnal amplitudes lag behind the semidiurnal amplitudes. In addition, D_2 becomes higher than D_1 during the last months at low river discharge (right panel).

Table 9: Amplitudes for diurnal, and semidiurnal tidal species and the corresponding tidal ranges at different gauge stations along the Kapuas River. Reference numbers correspond to the water level gauge map in the Annex.

Gauge Station	Reference Nr.	Distance from Sanggau [km]	High flow (10000m^3/s)			Low flow (1000m^3/s)		
			D_1 Amplitude [cm]	D_2 Amplitude [cm]	Range [cm]	D_1 Amplitude [cm]	D_2 Amplitude [cm]	Range [cm]
Sanggau	15796	0	1.93	0.81	4.85	27.16	17.40	78.78
Sungai Alai	5528	42	2.08	0.79	5.10	26.28	15.15	74.95
Meliau	5315	65.30	2.14	0.78	5.20	25.02	12.28	69.61
Kim Tayan	10691	91.10	2.21	0.80	5.35	23.14	8.40	61.96
Sungaidawat	10700	129	2.57	1.17	6.57	19.19	5.03	47.00
Mangis	10705	154.90	4.83	3.04	14.08	16.88	11.89	51.39
Terentang	10699	191.40	7.91	5.12	23.15	*17.17*	*19.48*	65.19
Teluk Bajur	10703	205.80	10.10	6.53	29.48	*18.83*	*21.65*	71.76
Chinese Temple (Delta apex)	10689	272.60	28.03	21.54	87.11	33.42	29.31	110.86

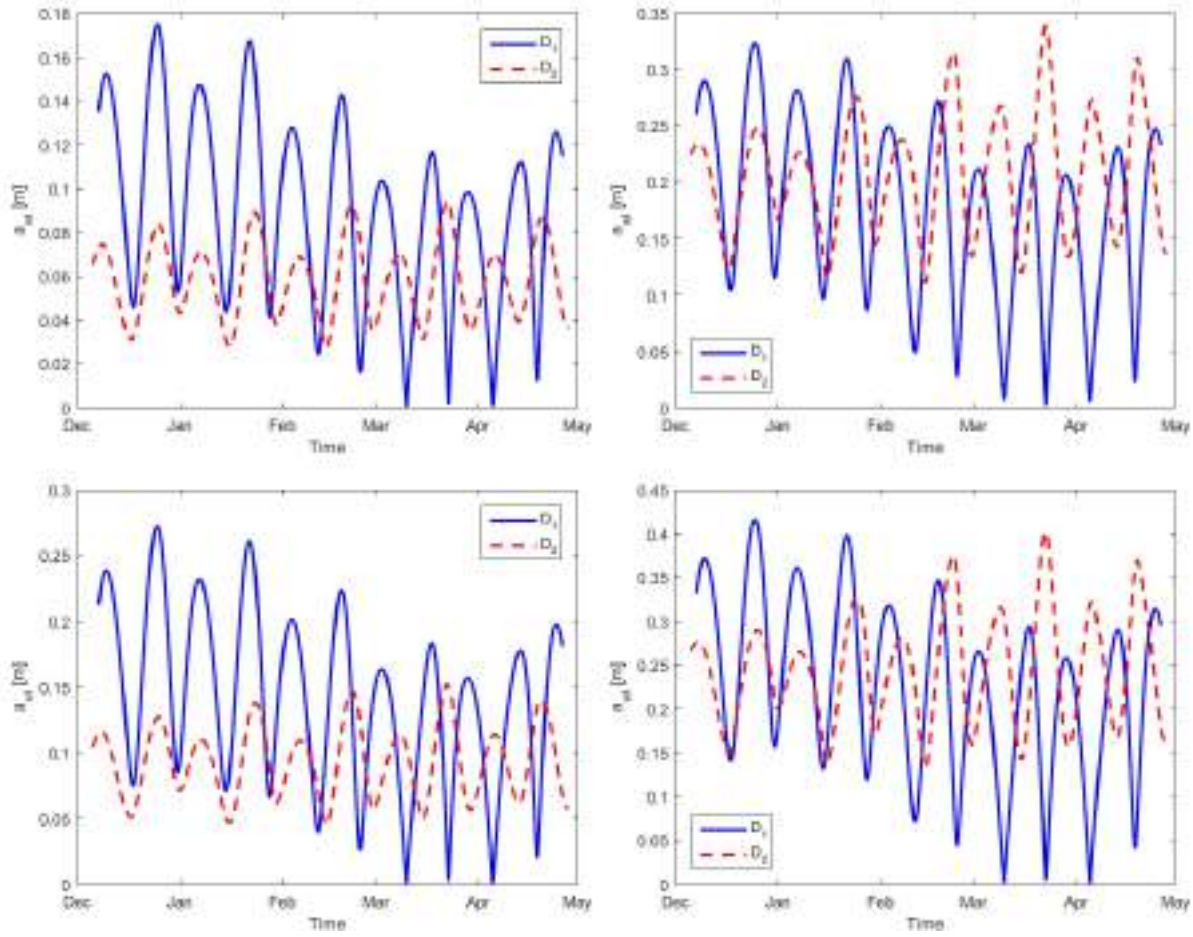

Figure 22: Diurnal (blue solid line) and semidiurnal tidal amplitudes (red dotted line) at the Kecil-Kapuas junction (top) and the Kubu-Kapuas junction (bottom) during high flow (left panel) and low flow (right panel).

It has been shown that tidal junctions are constrained by one water surface elevation even though flow velocities in the channels that connect the junctions are not necessarily the same [Buschman *et al.,* 2010]. Figures 46 and 47 in the Annex show the amplitudes of tidal velocities at the Kecil-Kapuas and Kubu-Kapuas junctions, respectively. It is worth noting that these amplitudes at the Kecil branch are close to zero, which may indicate that this junction acts as a natural barrier reflecting the tidal waves. This hypothesis is further developed in the last section.

7.1.3 Tidal amplitudes and phases

According to the D-FlowFM user's manual, [2017], observation points are linked to the closest nodes, and therefore, the grid needs a better refinement in order to interpolate co-range and co-tidal lines. Furthermore, it has been shown that the delay of high water is about 12 hours in 300km according to the field observations in the Kapuas River. Hence, co-range and co-tidal lines might be smoothed out and become inappreciable specifically at the junctions. Yet, it is possible to represent tidal amplitudes ($\sim$ half of the tidal range) and phases of the Kapuas. The tidal amplitudes and phases of the tidal constituents with the largest amplitudes (K_1 and M_2 - see Tables 7 and 8) are presented in Figures 23 and 24, respectively. In similar way, tidal amplitudes and phases of the other constituents can be found in the Annex (Figures 44 and 45).

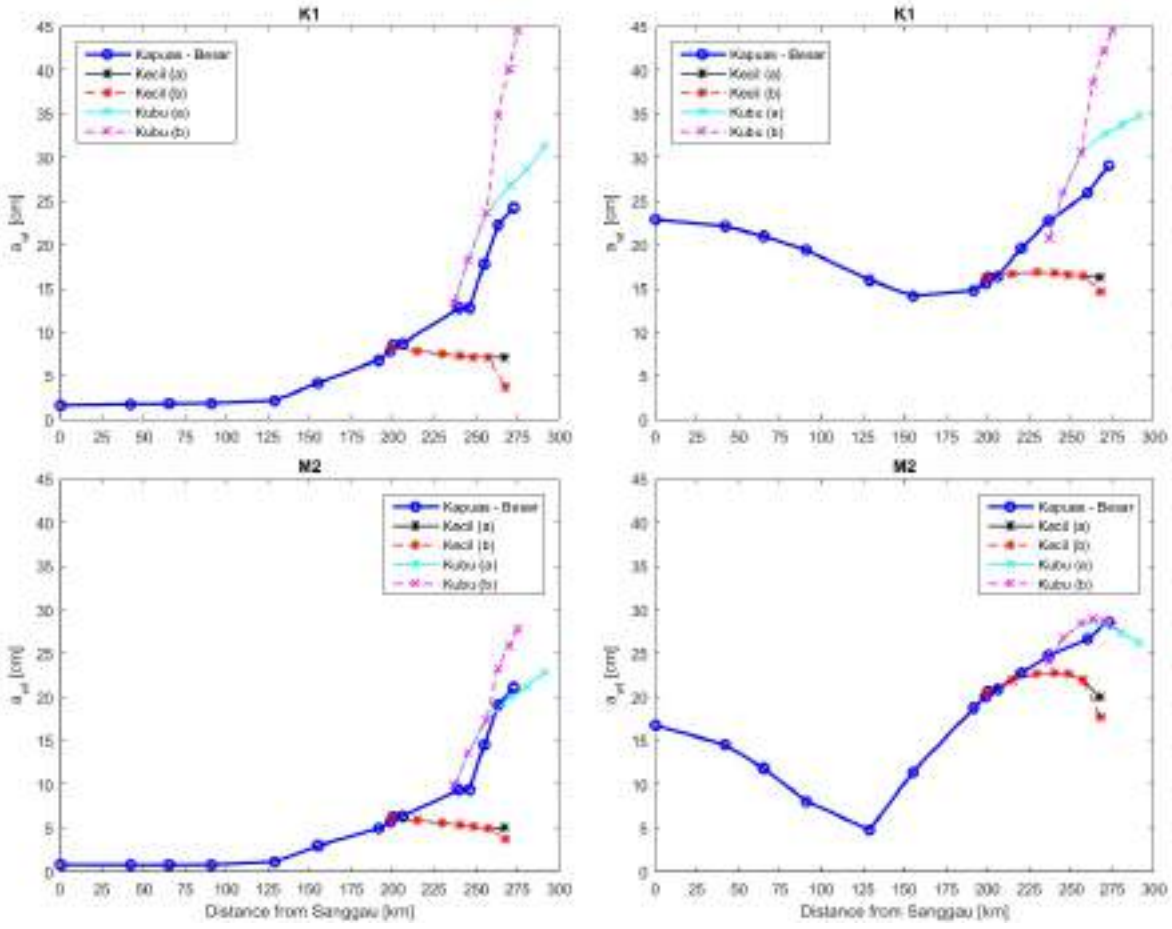

Figure 23: Tidal amplitudes of K_1 (top) and M_2 (bottom) along the main river channel and the Kapuas River branches for high flow (left panel) and low flow (right panel). Sub-indices (a) and (b) in the Kecil and Kubu branches indicate subdivision of the river branches at the sea.

During high flow, the tidal amplitudes of diurnal and semidiurnal constituents decrease in landward direction. However, the amplitudes in the Kecil branch increase upstream as can be seen in Figure 23 (red and black stars). The tidal amplitudes of M_2 at the junctions are slightly larger than the amplitudes of K_1 during low river flow. Likewise, during low river discharge, the tidal amplitudes decrease from the sea until kilometer 130, and unexpectedly, the tidal amplitudes increase towards the Sanggau station. This unusual behavior is analyzed in the next section. The same situation, as described above, hold for the other tidal constituents in the Annex.

The propagation of a tidal wave over the Kapuas River can be depicted by the tidal phase. Figure 24 illustrates the tidal phase at each gauge station and observation point. In general, the tidal phase increases in landward direction, which can be interpreted as the delay of high tide in upstream direction.

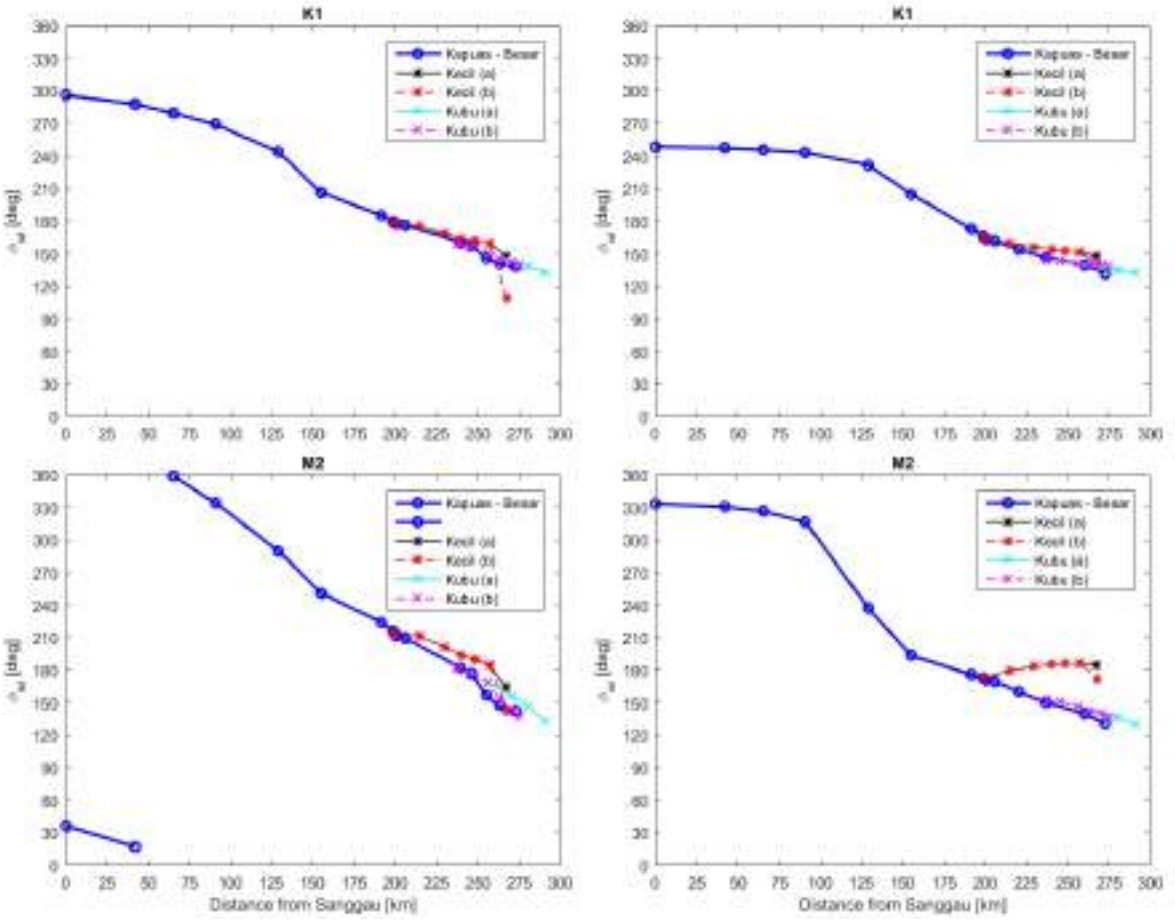

Figure 24: Tidal phase of K_1 (top) and M_2 (bottom) along the main river channel and the Kapuas River branches for high flow (left panel) and low flow (right panel). Sub-indices (a) and (b) in the Kecil and Kubu branches indicate subdivision of the river branches at the sea.

7.2 Tidal attenuation

Tidal attenuation is calculated as the ratio between the tidal ranges measured at any observation point on the Kapuas River respect to a fixed reference point at the sea. Under riverine influence, the tide can be either amplified or attenuated when tidal waves propagate in the river channel. In general, the effects of friction along the channel alter the tidal range by distorting the tidal waves [Buschman *et*

al., 2010]. Besides, it has been shown that increasing river discharge enhances tidal damping [Leonardi *et al.,* 2015]. Thus, high, medium and low river discharges are simulated in DELFT3D-FM® in order to assess the frictional effects and riverine influence on tidal attenuation. Tidal attenuation from field observations has been already calculated at the gauge stations as shown in Figure 25.

As mentioned in section 4.1, tidal amplitude and tidal range were obtained from wavelet analysis. These results can be seen in Table 9 for the Kapuas River, and for the Kecil and Kubu branches in Tables 10 and 11 in the Annex, respectively. The fixed tidal range *'r_o'* considered for computation of tidal attenuation corresponds to the most downstream observation point. This point is located at approximately 45km from the Chinese Temple gauge station as illustrated in Figure 38 in the Annex. The tidal attenuation from the model results along the main channel is presented in Figure 26. At low river discharge, tides are attenuated until kilometer 130 approximately, and eventually, they are amplified from that point to the Sanggau station.

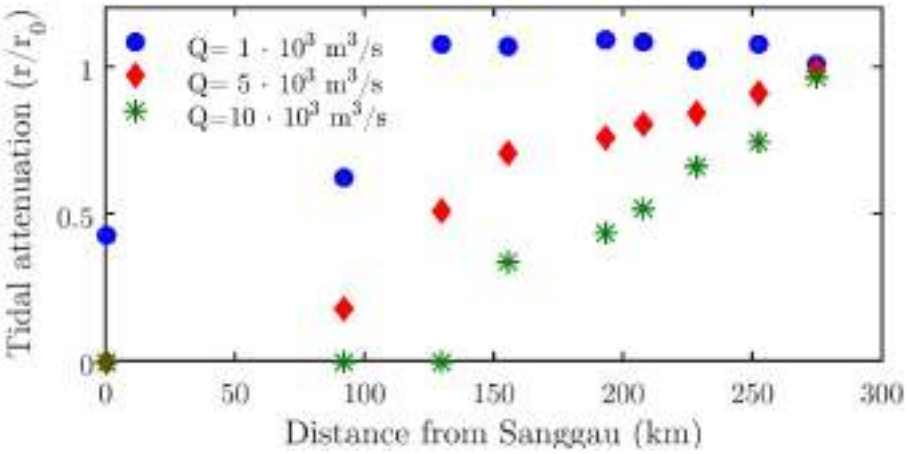

Figure 25: Tidal attenuation from field observations along the Kapuas River for high flow (blue dots), medium flow (red diamonds) and low flow (green stars). [Kästner et al., 2016].

Similarly, tidal attenuation along the river branches of the Kapuas are shown in Figures 39 to 41 in the Annex. Tidal attenuation in the Kecil branch (Figure 39) shows that the tides are amplified in the middle of the channel during low discharge. Likewise, the computation of tidal attenuation in the Kubu branch (Figures 40 and 41) clearly shows tidal damping as the tidal wave propagates in upstream direction.

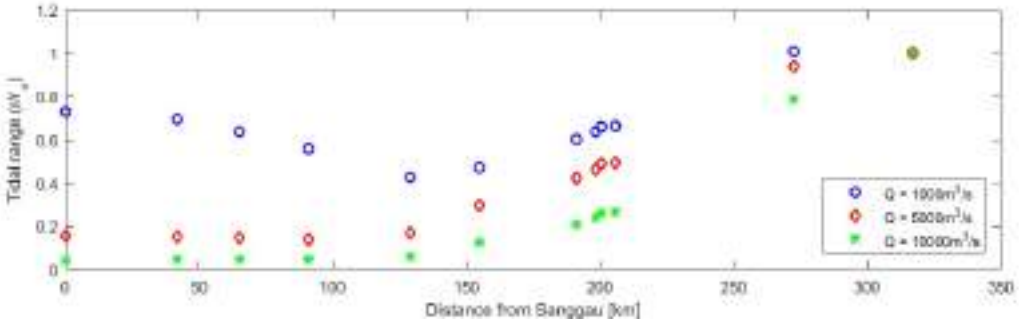

Figure 26: Tidal attenuation along the Kapuas River for high flow (blue empty dots), medium flow (red diamonds) and low flow (green stars).

7.2.1 Sensitivity analysis in terms of tidal attenuation

The motivation for performing this sensitivity analysis is the remarkable differences observed in tidal attenuation from field observations compared to model simulations. Fifty scenarios are run in DELFT3D-FM® in order to get the contribution of river discharge, bed roughness and mean bed level to the variance of the mean tidal attenuation value (i.e. computation of tidal attenuation is done for each time step and only the average of these results is considered). The sensitivity analysis is based on the model results at the Kecil-Kapuas junction, which is located at 198km approximately from the Sanggau station. The probability distribution of the mean tidal attenuation value at the junction is indicated in Figure 27. Additionally, the contribution of the three model parameters by means of their conditional expectation (i.e. prediction of the mean tidal attenuation value given a particular model parameter) is presented in Figure 28.

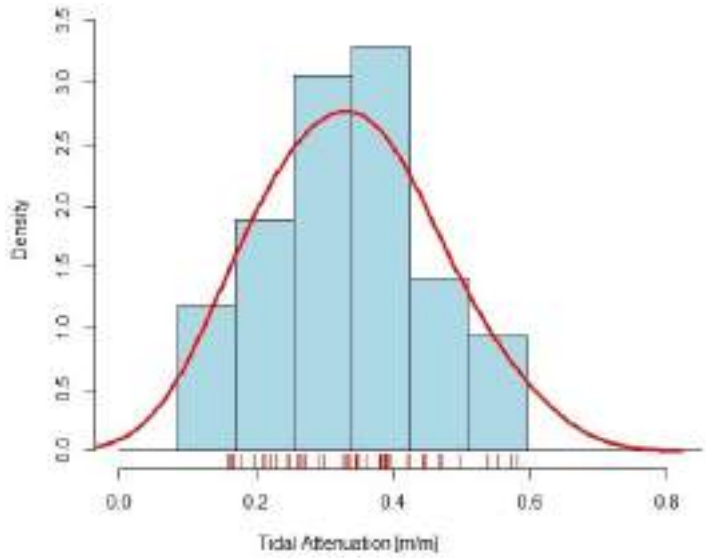

Figure 27: Histogram of tidal attenuation (blue rectangles) and its probability density (red line) at the Kecil-Kapuas junction.

Analysis of the histogram indicates that the mean tidal attenuation value for the fifty scenarios is 0.34 [-] with a standard deviation of 0.11 [-]. This value is close to the mean tidal attenuation value at medium river discharge (Figure 25). Figure 28 shows that river discharge and bed roughness are correlated with tidal attenuation. Positive correlation between Chézy friction coefficient and tidal attenuation suggests that tidal damping is low when the bed roughness is smooth. Negative correlation between river discharge and tidal attenuation indicates that tides are largely attenuated during high river flow. Likewise, the poor correlation between mean bed level and tidal attenuation may suggest that tidal damping is linked to the variation of cross section areas along the river channel and the corresponding bed slope rather than a single mean bed elevation for the entire Kapuas River. The pie chart shows an overview of the three model parameters and their individual contribution to the tidal attenuation value.

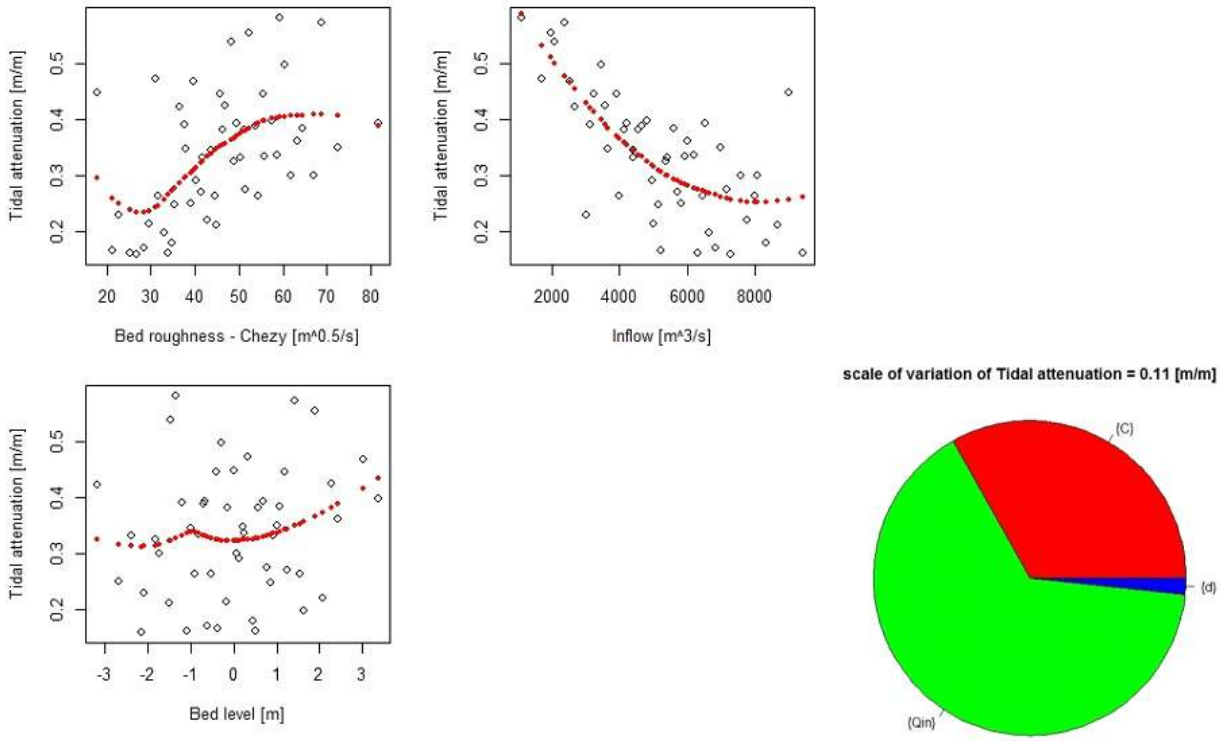

Figure 28: Left panel: Prediction of tidal attenuation as function of the three model parameters. Tidal damping is noticeable at low Chézy friction coefficients and high river discharges. Mean bed level has little influence on tidal attenuation. Right panel: Pie chart of total scale of variation due to river discharge (Q_{in}- green), bed roughness (C- red) and mean bed level (d - blue). The main sources of tidal damping are river discharge and bed roughness.

7.3 Tidal energy

As indicated in section 3.2.2, tidal energy is conveyed by progressive waves until becoming extinct due to bottom friction effects and riverine flow. At tidal junctions, the tidal energy might act in three different ways. For instance, the tidal energy flux coming from the sea and propagated along a river branch and the main river channel can be added up, and as a result, the resulting tidal energy flux propagates in upstream direction. Another possibility is that the energy fluxes might be locally dissipated in the channel at the downstream part of the junctions. A third situation may occur in which part of the tidal energy coming from one channel makes a U-turn towards the second channel, while the rest of the energy propagates upstream.

The equation of energy flux proposed by Gill, [1982] is used to estimate the tidal energy at the channels connected by the junctions. This equation requires water depth and flow velocities from the simulation results. Figures 20 and 21 show the observation points and cross sections placed in both junctions to record the output model results for high and low river flow.

Some pre-processing steps are required before applying the energy flux equation. The water depth, from each observation point in the junction, have to be averaged out over 25 hours approximately (one lunar day). In that way, the water surface elevation can be calculated with a floating mean. Furthermore, it is assumed that the water depth remains constant along the three cross sections of the junction. Although the bathymetry does vary along the cross section, each observation point stores

the water depth at the nearest node (see D-FlowFM user's manual, [2017]). Flow velocities on the other hand, represent the cross section velocity of the channel. These velocities are automatically computed by DELFT3D-FM® at each time step. In that way, $\overrightarrow{F}$ represents the tidal energy flux per unit width at the nearest node from the mesh, and for that reason, it is handy to define the total tidal energy transport across the channel section, as follows.

$$\overrightarrow{E} = \frac{\rho g H w}{T} \int_0^T \zeta \overrightarrow{u} \, \mathrm{d}t \tag{8}$$

where '$\overrightarrow{E}$' is the total energy flux [W], and 'w' is the width of the channel calculated as the ratio of cross section area to water depth at each time step. The derivation of this equation is included in the Annex.

Figures 29 and 30 show the total energy flux in both junctions for high and low river flow, respectively. Tidal energy at the sea propagates into the Kapuas River through the Besar distributary and the Kubu branch. These tidal energy fluxes are added up at the Kubu-Kapuas junction, and the resulting tidal energy propagates through the Kapuas upstream cross section for both high and low river discharge (Figure 29). The incoming and outgoing tidal energy fluxes are balanced, which implies that the sum of the tidal energy at the junction is close to zero. Moreover, the magnitude of the tidal energy flux is larger at spring tides than at neap tides. Besides, the Kubu branch adds to the Kapuas River a mean tidal energy flux of 103 [KW] and 789 [KW] during high and low river flow, respectively. Similarly, the mean tidal energy flux transmitted from this junction in upstream direction is 447 [KW] at high river flow, and 4.40 [MW] at low river flow.

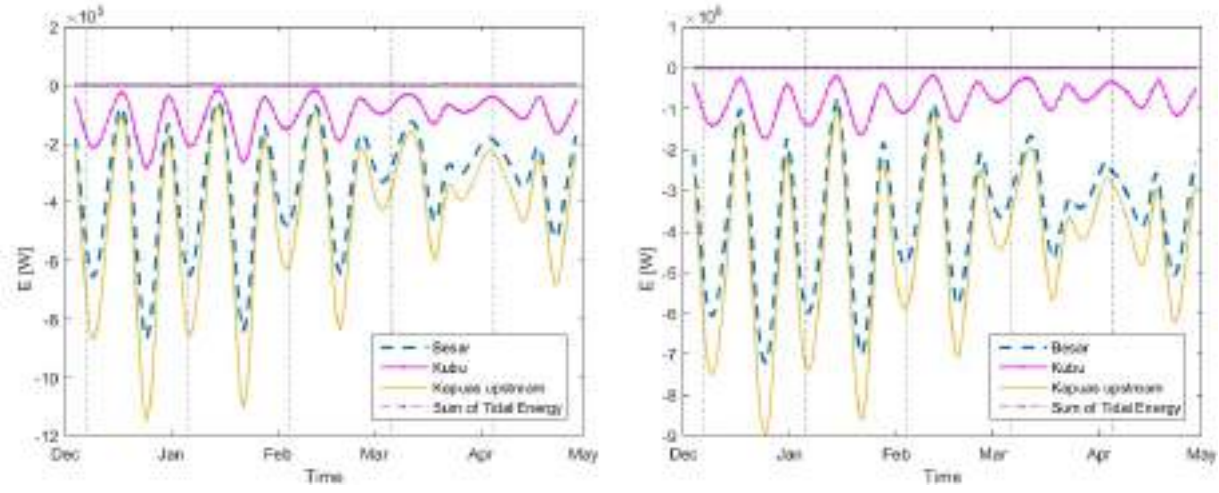

Figure 29: Tidal energy flux over the cross sections of the Kubu-Kapuas junction for high flow (left panel) and low flow (right panel). Black dotted lines represent full moon days. Negative values indicate inflow tidal energy in landward direction, while positive values indicate outflow tidal energy in seaward direction.

The resulting tidal energy from the Kubu-Kapuas junction propagates in landward direction as well as the tidal energy coming from the Kecil branch. However, the tidal energy in that river branch is redirected in seaward direction during high river discharge (Figure 30 - left panel). As a result, the resulting tidal energy propagates in landward direction, but its magnitude is lesser than the tidal energy coming from the downstream junction. The tidal energy coming from that junction is splitted

up at the Kecil-Kapuas junction, and the incoming and outgoing tidal energy fluxes are in balance. Besides, the Kecil branch receives more tidal energy at spring tides than at neap tides. The mean tidal energy flux drained by the Kecil branch is about 27 [KW]. Additionally, the mean tidal energy flux received from the downstream junction is 220 [KW] and the mean tidal energy flux transmitted by this junction in upstream direction is 192 [KW].

The tidal energy transported by the Kecil branch presents a singular behavior during low river discharge (Figure 30 - right panel). From December to the middle of February, the Kecil branch adds tidal energy to the Kapuas River. After this first period, the tidal energy is seaward directed and the Kecil branch drains tidal energy from the main channel. The magnitude of the tidal energy flux is larger at spring tides than at neap tides. Furthermore, in the first period the Kecil branch adds a mean tidal energy flux of 93 [KW], and posteriorly, it drains a mean tidal energy flux of 66 [KW]. Similarly, the mean tidal energy flux received from the downstream junction is 3.38 [MW] and the mean tidal energy flux transmitted by this junction in upstream direction is 3.40 [MW].

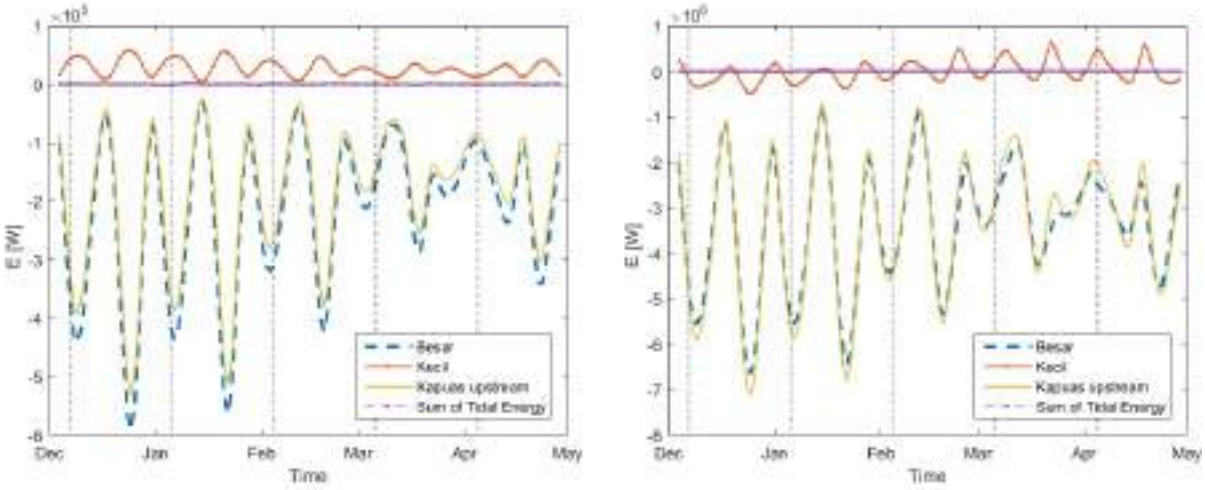

Figure 30: Tidal energy flux over the cross sections of the Kecil-Kapuas junction for high flow (left panel) and low flow (right panel). Black dotted lines represent full moon days. Negative values indicate inflow tidal energy in landward direction, while positive values indicate outflow tidal energy in seaward direction.

Figures 29 and 30 present another peculiarity. From December to the middle of February, the tidal energy presents a smooth cyclicity related to the spring-neap cycle. After that period, the tidal energy flux decreases and the cyclicity becomes irregular. The changes of tidal energy magnitude and irregular cyclicity coincide with the months at which the amplitude variation of water level, for both diurnal and semidiurnal tides, are out of phase (Figure 22) and are discussed in the last section.

7.4 Discharge distribution

Discharges at the Kecil-Kapuas and Kubu-Kapuas junctions are calculated from the model results at the cross sections indicated in Figures 20 and 21. The subtidal discharge is quantified in terms of the discharge asymmetry index and compared to the subtidal water level at the junctions.

7.4.1 Discharge asymmetry index

The discharge asymmetry index *'Ψ'* is defined as the difference in subtidal discharge between two channels and divided by their sum. The definition follows the approach of Buschman *et al.,* [2010].

$$\Psi = \frac{< Q >_1 - < Q >_2}{< Q >_1 + < Q >_2} \tag{9}$$

$< >$: indicates tidal average (over one lunar day ∼25 h).

The discharge asymmetry index can present singular values:

+1: All subtidal discharge flows through the narrow channel (river branch).

0: Subtidal discharge has an equal division in both channels.

-1: All subtidal discharge flows through the wider channel (main river channel).

The subtidal water level *'η'* is calculated by averaging the time series of water level over one lunar day.

Figure 31 presents the subtidal discharge distribution and the subtidal water level at the Kubu-Kapuas junction. During high river discharge (left panel), Ψ remains almost invariable (-0.638 [-] as average) for the entire simulation period, and as a result, the river discharge is allocated to the Kapuas River (main channel). During low river discharge (right panel), Ψ has a large variation with a maximum value of -0.55 and a minimum value of -0.77 roughly. Besides, it can be seen that η features a spring-neap oscillation directly in response to the tidal forcing. The subtidal discharge distribution peaks at neap tides, which implies that less river discharge is allocated to the main channel, and the Kubu branch increases its discharge. At spring tides the opposite occurs, the subtidal discharge distribution reaches its lowest values, and a greater river discharge is allocated to the Kapuas River.

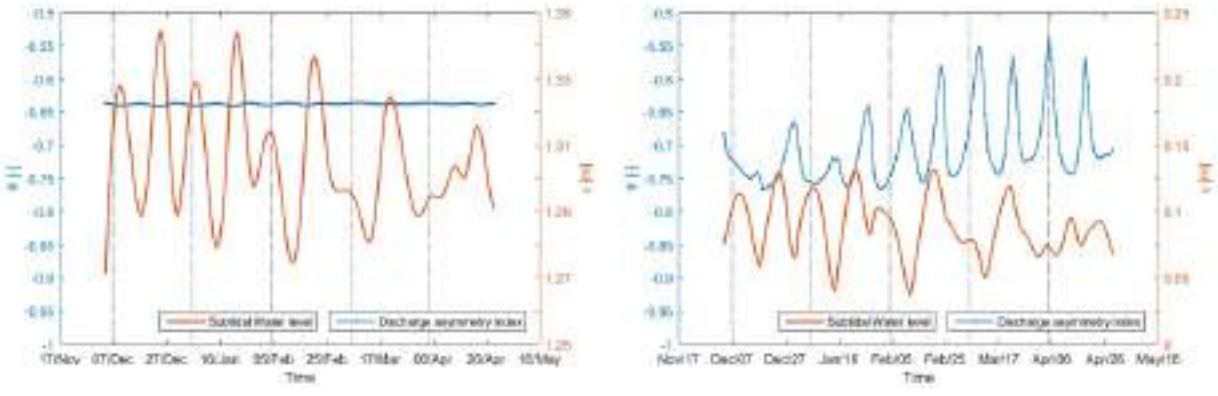

Figure 31: Discharge asymmetry index Ψ (blue dotted line) and subtidal water level η (orange solid line) at the Kubu-Kapuas junction for high flow (left panel) and low flow (right panel). Black dotted lines represent full moon days.

Figure 32 presents the subtidal discharge distribution and the subtidal water level at the Kecil-Kapuas junction. During high river discharge, Ψ presents an average value of -0.54 [-] which indicates that the river discharge is allocated to the main channel. During low river discharge, Ψ has a maximum

value of -0.66 and a minimum values of -0.92 roughly. Besides, it can be seen that the subtidal discharge distribution resembles the spring-neap oscillation of the subtidal water level. In general, Ψ lags behind η and peaks at the transition between neap tide and spring tide. The transition between spring tide and neap tide is relevant at this junction though. The subtidal discharge distribution gets values close to -0.90 at this transition, which indicates that almost the entire river discharge flows through the main channel.

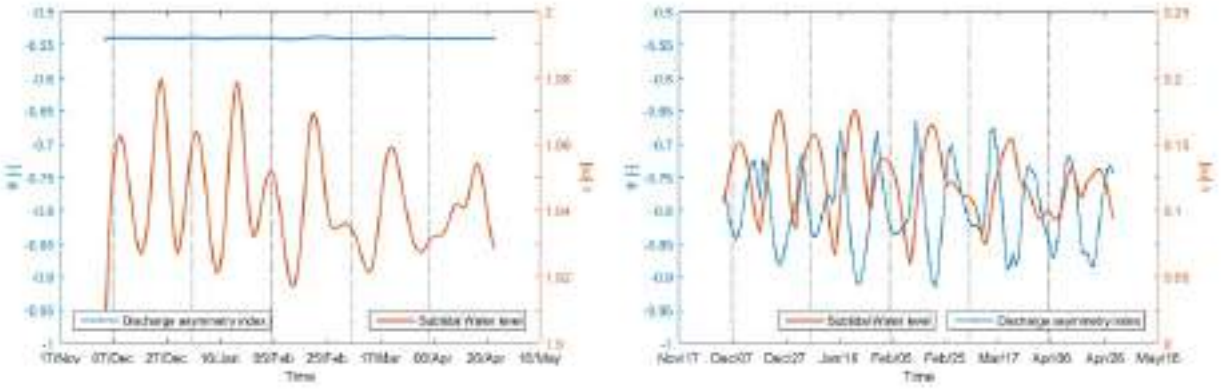

Figure 32: Discharge asymmetry index Ψ (blue dotted line) and subtidal water level η (orange solid line) at the Kecil-Kapuas junction for high flow (left panel) and low flow (right panel). Black dotted lines represent full moon days.

7.4.2 Sensitivity analysis in terms of subtidal discharge distribution

In order to assess the influence of river discharge *'Q_{in}'*, bed roughness *'C'* and mean bed level *'d'* at the junctions, sensitivity analysis based on the subtidal discharge distribution value is proposed. The procedure is the same as the one carried out for tidal attenuation (see section 7.2.1). The probability distribution and conditional expectation of the three model parameters at the Kecil-Kapuas junction are indicated in Figures 33 and 34.

Analysis of the histogram indicates that the mean Ψ value for the fifty scenarios is 0.58 [-] with a standard deviation of 0.06 [-]. These values indicate that the river discharge is mainly allocated to the Kapuas River (main channel). Figure 34 (left panel) shows that river discharge and bed roughness are strongly correlated with Ψ. Negative correlation between bed roughness and Ψ suggests that the discharge asymmetry index decreases when the Chézy friction coefficient reaches high values. Therefore, the smoother the bed roughness the more river discharge is allocated to the main channel. Positive correlation between river discharge and Ψ suggests that less river flow is allocated to the main channel when the river discharge increases. Likewise, the poor correlation between mean bed level and Ψ suggests that any change in the mean bed elevation does not influence the allocation of river flow to either the Kapuas River or the Kecil branch. The pie chart shows an overview of the three model parameters with their individual contribution to the subtidal discharge distribution.

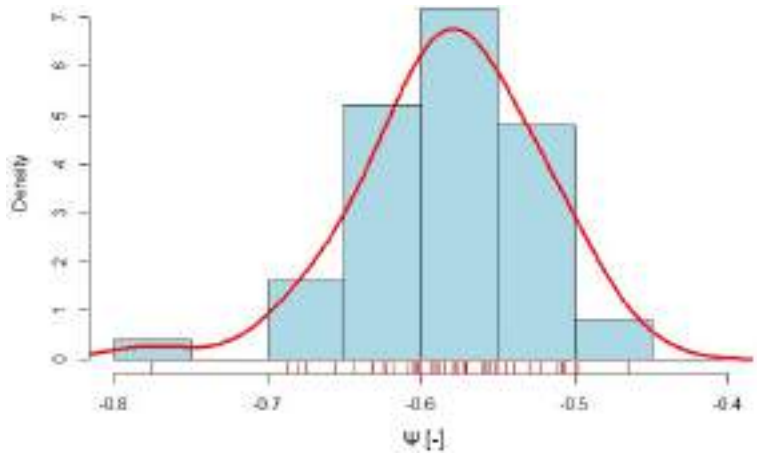

Figure 33: Histogram of the mean discharge asymmetry index (blue rectangles) and its probability density (red line) at the Kecil-Kapuas junction.

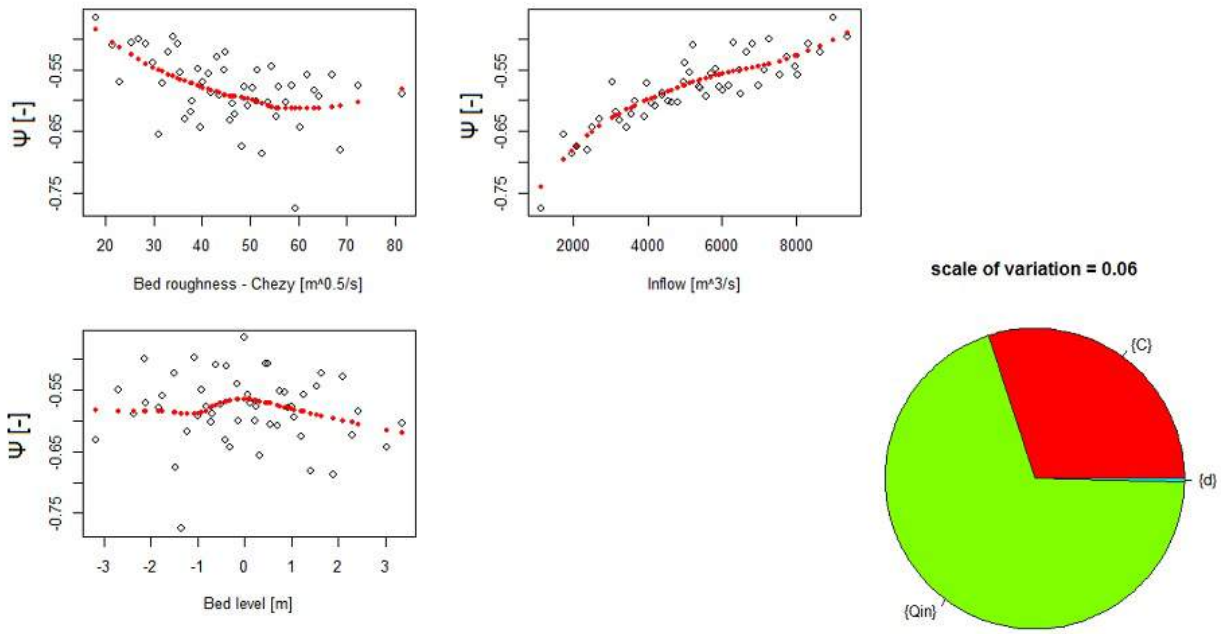

Figure 34: Left panel: Prediction of discharge asymmetry index as function of the three model parameters. Right panel: Pie chart of total scale of variation due to river discharge (Q_{in}- green), bed roughness (C- red) and mean bed level (d - blue).

In the same way, the results for the Kubu-Kapuas junction are presented in Figures 35 and 36. Analysis of the histogram indicates that the mean Ψ value for the fifty scenarios is -0.65 [-] with a standard deviation of 0.01 [-]. These values indicate that the river discharge is mainly allocated to the Kapuas River (main channel). Figure 36 (left panel) shows that river discharge and bed roughness are correlated with Ψ. The mean bed level and Ψ indicate a poor correlation as it was described for the Kecil-Kapuas junction. The pie chart shows an overview of the three model parameters with their individual contribution to the subtidal discharge distribution.

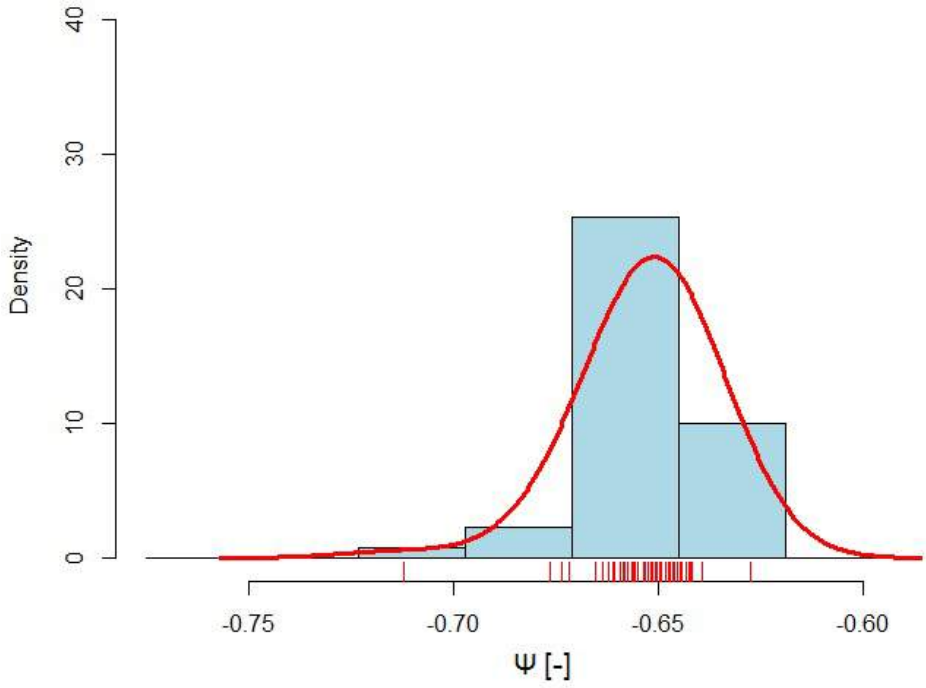

Figure 35: Histogram of the mean discharge asymmetry index (blue rectangles) and its probability density (red line) at the Kubu-Kapuas junction.

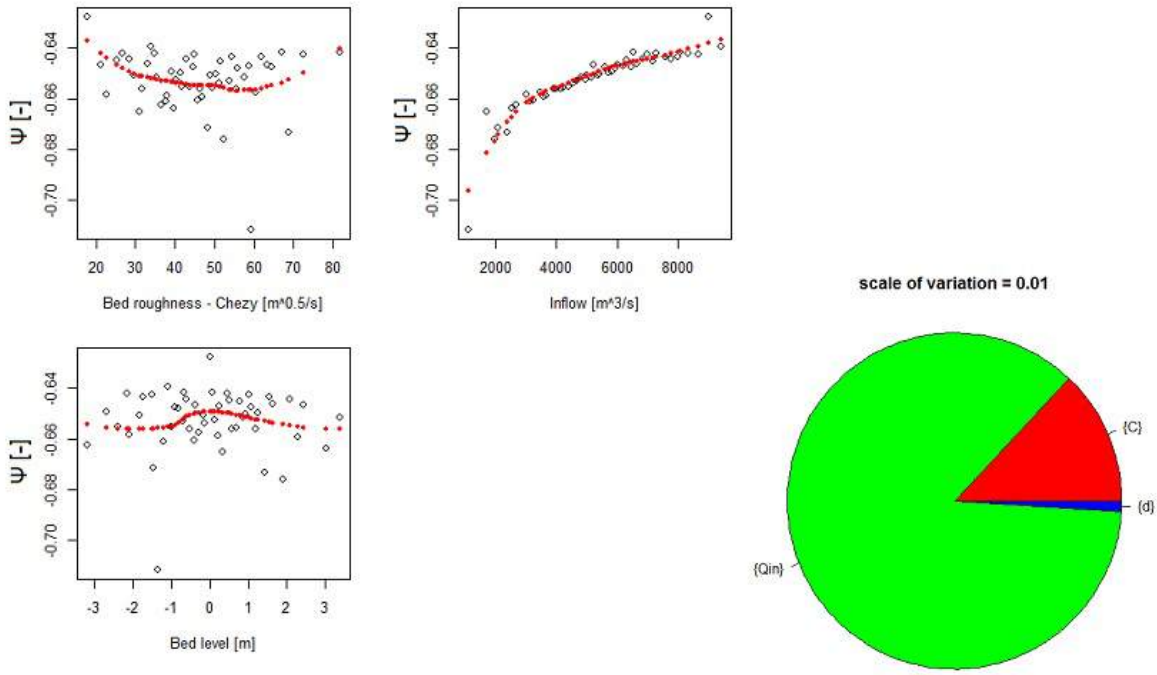

Figure 36: Left panel: Prediction of discharge asymmetry index as function of the three model parameters. Right panel: Pie chart of total scale of variation due to river discharge (Q_{in}- green), bed roughness (C- red) and mean bed level (d - blue).

8 Discussion

Figures 25 and 26 illustrate the tidal attenuation along the Kapuas River calculated from field-observations and model simulations, respectively. Differences in magnitude of tidal attenuation are evident when the figures are compared to each other. During high and medium river discharges, the tides are more attenuated in the model simulations than in reality. From sensitivity analysis (see Figure 28), it was shown that tidal damping is strong when the Chézy friction coefficient reaches low values (i.e. when the river bed is coarse). Therefore, the strong attenuation experienced by the tides in the simulations could be attributed to a relatively high bed roughness assigned to the Kapuas River in the model. According to Buschman *et al.,* [2010], high bed roughness in river channels results in smaller tidal ranges, and as a result, the tidal wave is more distorted.

Tidal attenuation at low river discharge shows a singular behavior, though. The tides are attenuated as in high and medium river discharge, but suddenly, they are amplified from kilometer 130 to the upstream boundary at Sanggau. This particular behavior is also seen in Figures 23 and 44 (left panel). As it was mentioned in section 7.1, the model simulation ran for 5 months which does not fully satisfy the Rayleigh criterion. Therefore, amplitudes and phases of water levels and flow velocities may not be properly captured at certain locations from either harmonic or wavelet analysis, especially at low river flow where the tidal amplitudes become larger. Another possible explanation is artificial reflection of the tidal wave at the upstream boundary of the Kapuas River. The tidal energy is not completely dissipated from the Kecil-Kapuas junction to Sanggau at low flow, as shown in Figure 49 in the Annex. If the tidal energy is not able to leave the upstream boundary and to continue until becoming extinct further upstream, reflection of the tidal wave may be causing amplification in the first 130km of the Kapuas River. In addition, it may be possible that the Mendawat branch (Figure 1) is adding tidal energy to the river system similar to the Kecil and Kubu branches. However, the latter is only an hypothesis since the analysis of tidal energy flux at this junction was omitted in the present study.

Tidal amplification at low flow in the Kecil branch (see Figure 39 in the Annex) may indicate that the river branch is a convergent channel, and consequently, the tides are amplified in landward direction due to funneling [Van Rijn, L. C., 2010]. Despite the increase in depth of the Kecil branch, the channel area and channel width of the Kecil decrease as tides propagates upstream, which confirm the hypothesis of convergence in this river branch (see Figure 48 in the Annex). At high river discharge, the tides are attenuated as expected. However, the tides experience a slight amplification at the Kecil-Kapuas junction, which is also seen in Figure 23 (left panel). Besides, the amplitudes of flow velocities at the Kecil branch (close to the junction) are almost zero for both diurnal and semidiurnal tides at high river discharge (see Figure 46 - left panel). It has been shown that some estuaries, whose lengths equal a quarter of wavelength and their natural periods coincide with the periods of the tidal forcing, experience resonance effects [Pugh and Woodworth, 2014]. Thus, the channel length of the Kecil branch may be also controlling the propagation and reflection of the tidal wave energy as shown in similar studies of flow division [Buschman *et al.,* 2013] . These theoretical concepts (i.e. standing waves and resonance) may corroborate the hypothesis of reflection at the Kapuas-Kecil junction. This junction may be acting as a natural barrier, and therefore, the tides are amplified and reflected in seaward direction.

On the other hand, sensitivity analysis in terms of discharge asymmetry index suggests the smoother the bed roughness in both channels, the more river discharge is allocated to the main channel. This can be explained by comparing the bed level of the main channel and the river branches. Buschman *et al.,* [2010] showed that tidal motion generally favors the allocation of river discharge to deeper channels, enhancing the inequality in discharge distribution that would occur due to river flow. At the junctions, there is a difference in depth of approximately 3 and 8m for the Kecil-Kapuas and Kubu-Kapuas, respectively (see Figure 48). Therefore, the river discharge is allocated to the main channel

due to the larger depth. Likewise, the sensitivity analysis showed that less river flow is allocated to the main channel when the river discharge increases. According to Sassi *et al.,* [2011], the channel that conveys larger share of the river discharge exhibits a tendency to generate a subtidal water setup at the junction. Although the junction is constrained by one water surface level, the deeper channel increases the subtidal water level at the junction towards the smaller and shallower channel. This phenomenon termed *'differential water level setup'* is triggered by the river discharge-tide interaction in the deeper channel. The latter may explain the allocation of river discharge to the Kecil and Kubu branches when the flow increases and attenuates the tidal propagation in the Kapuas River.

9 Conclusion

Tidal energy at the junctions indicates that the Kubu branch has a greater impact on the energy budget of the Kapuas River than the Kecil branch (see Figures 29 and 30). Despite of the relative small area of the Kubu branch, it adds a mean tidal energy flux of 789 [KW] at low river flow, and 103 [KW] at high river flow. The Kecil branch on the other hand, adds a mean tidal energy of 13.50 [KW] at low river flow and drains 27 [KW] at high river flow. The change of mean tidal energy in the Kecil branch might be related to the larger amplitudes of water level from December to the middle of February (see Figure 22 - left panel). The energy flux equation considered in this study depends mainly on the surface water elevation and flow velocities as indicated in section 7.3. Consequently, the tidal energy flux will be largely determined by the amplitudes of water level provided that the mean flow velocity and the corresponding diurnal and semidiurnal velocity amplitudes remain constant (Figure 46 - left panel). In this particular period, the tidal energy flux is negative which implies that the Kecil branch adds tidal energy to the river system.

The tidal energy dissipated from the upstream part of the Kubu-Kapuas junction to the downstream part of the Kecil-Kapuas junction is about 51% (227 [KW]) at high river flow, and about 23% (1 [MW]) at low river flow. Hence, these results may indicate that the tidal energy in the Kapuas River is mainly dissipated by riverine influence rather than bottom friction effects. High river discharges attenuate the tides by a factor of 2 with constant bed roughness along the Kapuas River. The latter is corroborated by other studies where the river discharge acts to redistribute and dissipate tidal energy, due to the strong effect of a net flow on friction [Buschman *et al.,* 2010 & Godin and Martínez, 1994]. Moreover, according to Leonardi *et al.,* [2015], the presence of a river discharge has the same effect than increasing friction by a factor proportional to the riverine to the tidal discharge ratio. Concerning the distribution of tidal energy, it may be dissipated around isolated topographic features (e.g. valleys or sudden prominences in the river bed) rather than uniformly distributed as stated by Zhong and Li, [2006].

Figures 31 and 32 indicate the subtidal discharge distribution at the Kubu-Kapuas and Kecil-Kapuas junctions, respectively. Buschman *et al.,* [2010] reported that subtidal discharge division tends to become more unequal with increasing tidal range. In the same way, the most relevant results in this study arise from low river flow where the discharge asymmetry index varies significatively due to the presence of large tidal amplitudes at the junctions (see Figures 23 and 44). At the downstream junction, allocation of the maximum river discharge to the Kubu branch occurs at neap tides, when the tidal energy flux added by this branch is less than spring tides (Figure 29 - left). At the upstream junction however, the transition between neap and spring tides determines the allocation of maximum river discharge to the Kecil branch. Surprisingly, the river discharge flowing in the Kecil branch is relatively low at the transition between spring to neap tides (Ψ = -0.90 [-]). The tidal energy drained by this branch peaks at neap tides. At spring tides however, this branch adds tidal energy to the river system (Figure 30 - right panel).

Further research is advised in order to fully understand the influence of tides in the flow division at the junctions of the Kapuas River. After a proper model calibration, it is suggested to assign individual bed friction coefficients to the river branches rather than considering a single Chézy coefficient for the entire model. In addition, the bottom friction could be segmented by discriminating fluvial parts, distributaries and deep water in the model domain as proposed by Sassi *et al.,* [2011]. The latter could diminish the excessive tidal attenuation along the Kapuas River. Likewise, it is suggested to conduct a sensitivity analysis by varying the individual bed roughness of the channels. The latter could validate the findings of Buschman *et al.,* [2010]. They stated that tidal motion induces a net discharge from the channel with low bed roughness to the channel with higher bed roughness. Finally, analysis of tidal energy distribution and dissipation in the Kapuas River may reveal the intriguing

shape of the junctions.

10 Annex

Figure 37: Water level gauge map of the main river channel and the Kapuas River branches. Reference numbers correspond with Table 9. Adapted from [Kästner, 2016].

Figure 38: Observation points (eye-icon) placed along the Kapuas River and the Kecil and Kubu branches for model simulation in DELFT3D-FM®. The observation point located at the South China Sea (red circle) is the fixed reference point.

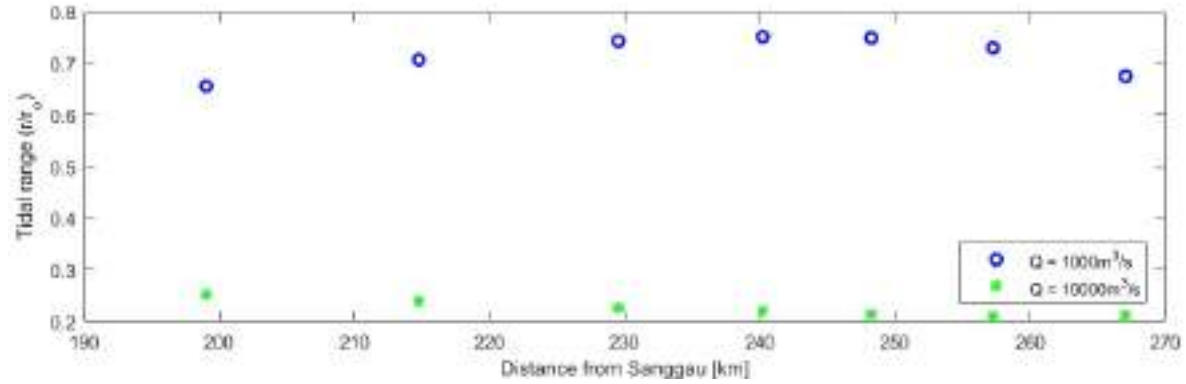

Figure 39: Tidal attenuation along the Kecil branch for high flow (blue empty dots) and low flow (green stars).

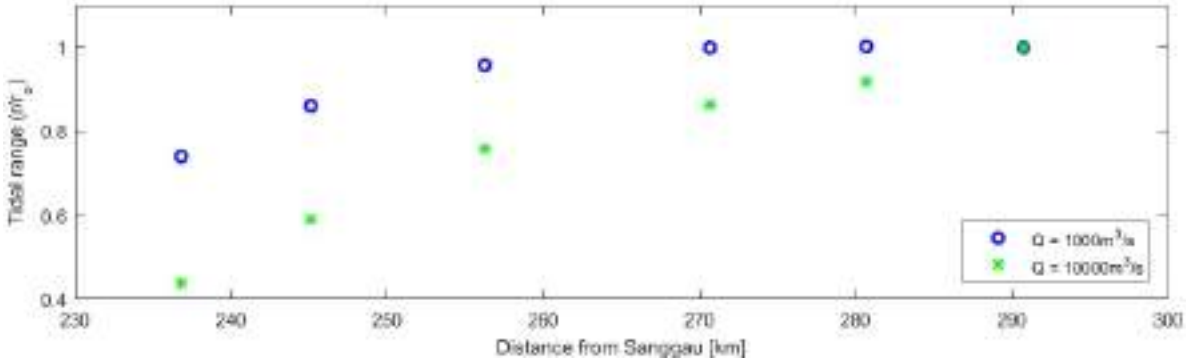

Figure 40: Tidal attenuation along the Kubu branch for high flow (blue empty dots) and low flow (green stars).

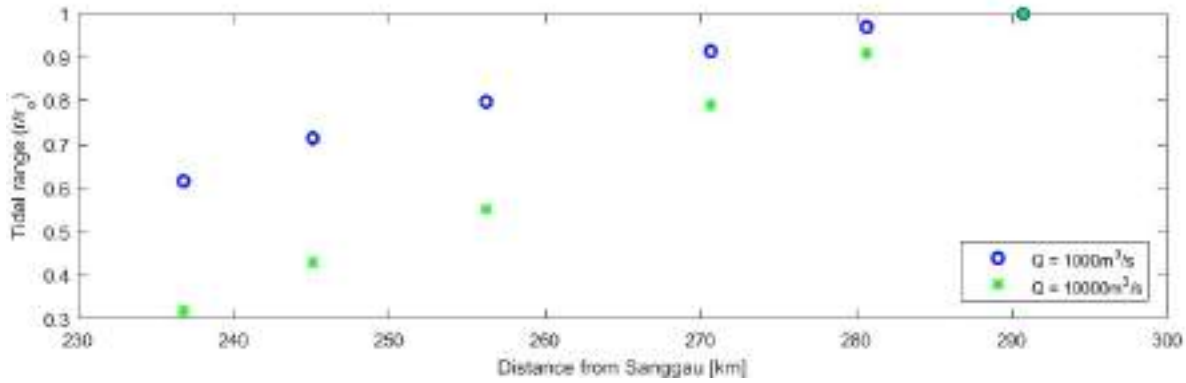

Figure 41: Tidal attenuation along the Kubu branch (b) for high flow (blue empty dots) and low flow (green stars).

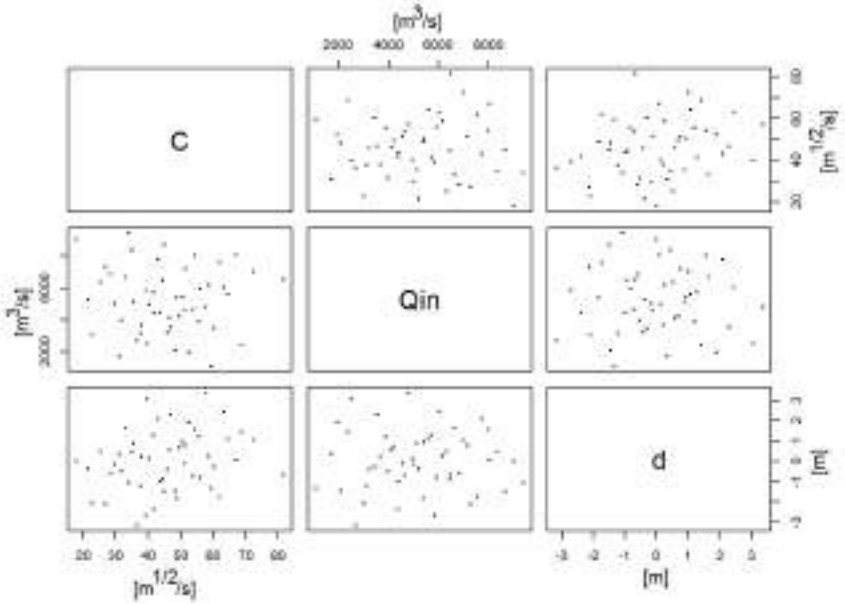

Figure 42: Parameter samples of bed roughness (C), river discharge (Q_{in}) and mean bed level (d) created by the Latin Hypercube sampling technique.

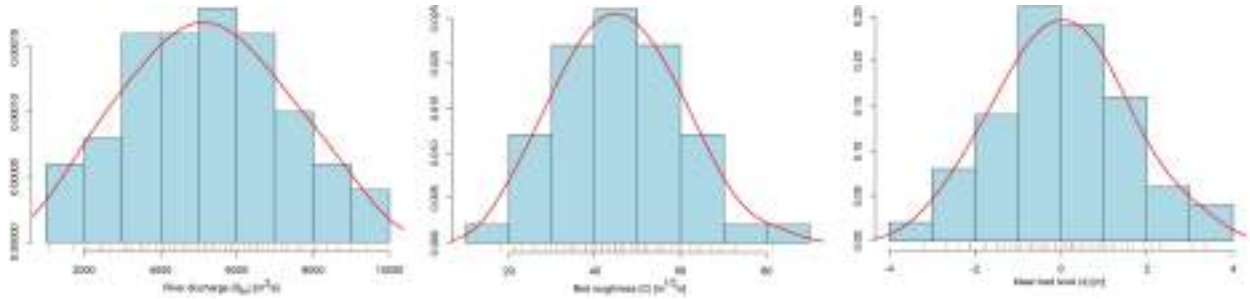

Figure 43: Histogram of the river discharge sample (left), bed roughness (middle) and mean bed level (right), and their probability density (red lines) created for sensitivity analysis.

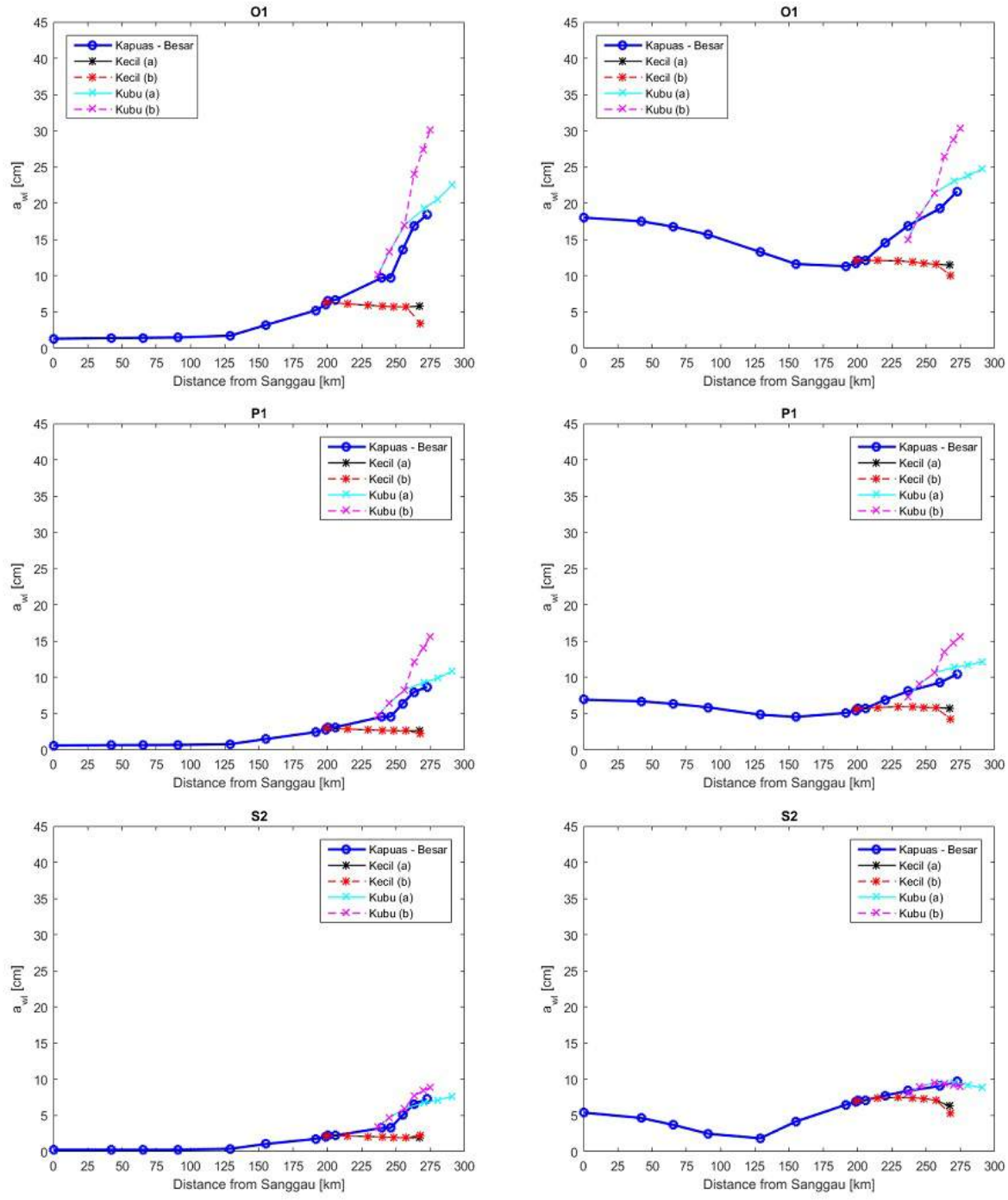

Figure 44: Tidal amplitudes of O_1 (top) P_1 (center) and S_2 (bottom) along the main river channel and the Kapuas River branches for high flow (left panel) and low flow (right panel). Sub-indices (a) and (b) in the Kecil and Kubu branches indicate subdivision of the river branches at the sea.

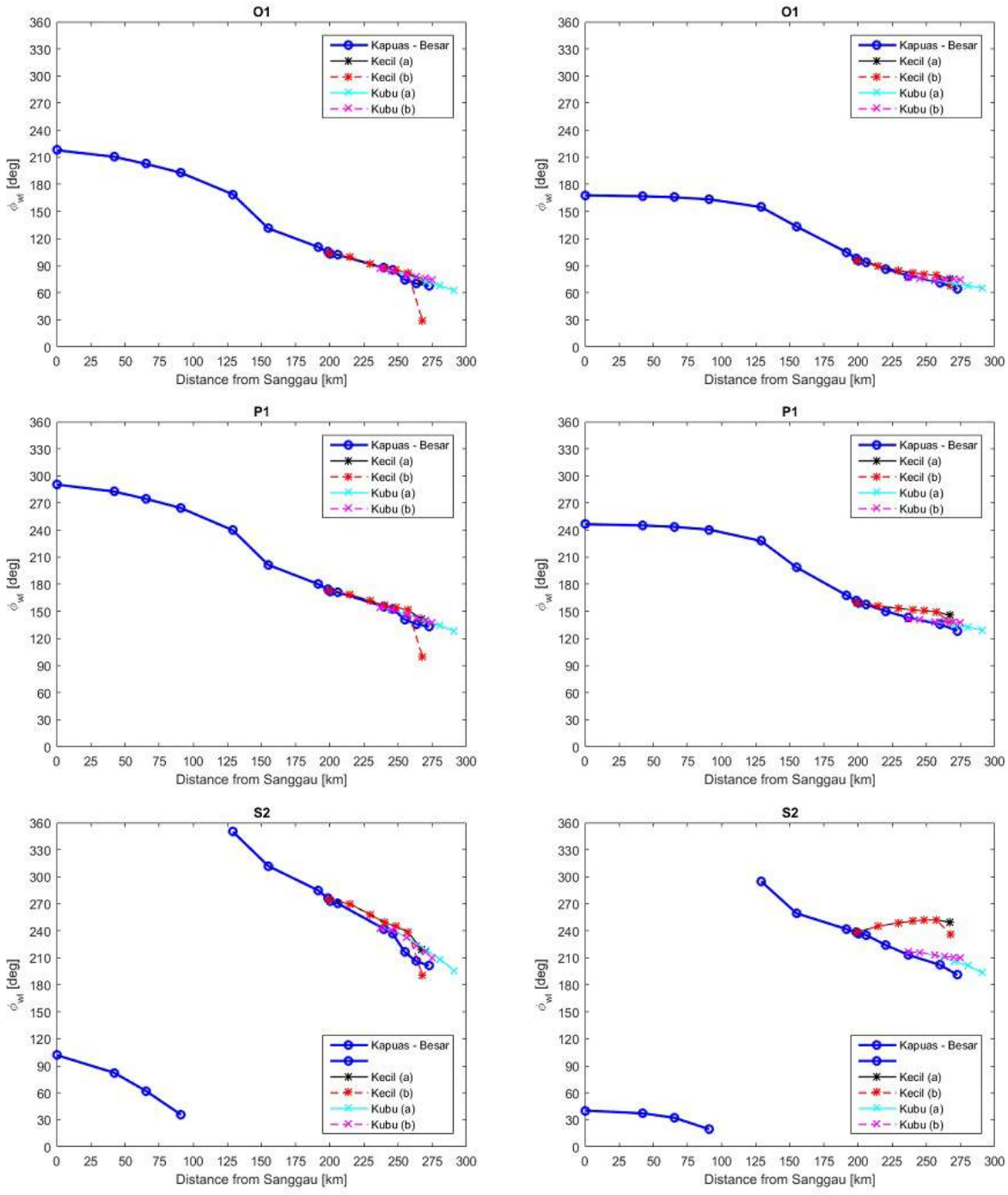

Figure 45: Tidal phases of O_1 (top) P_1 (center) and S_2 (bottom) along the main river channel and the Kapuas River branches for high flow (left panel) and low flow (right panel). Sub-indices (a) and (b) in the Kecil and Kubu branches indicate subdivision of the river branches at the sea.

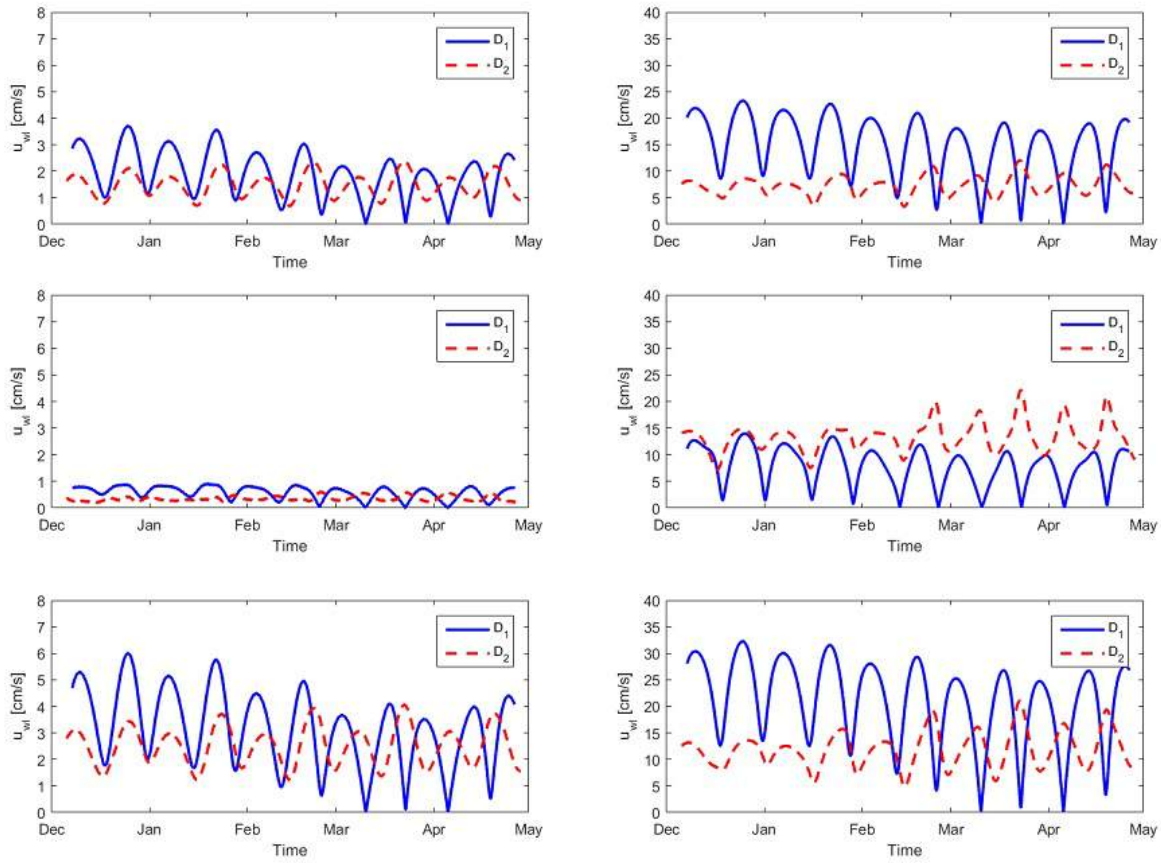

Figure 46: Diurnal (blue solid line) and semidiurnal velocity amplitudes (red dotted line) during high flow (left panel) and low flow (right panel) at the Kecil-Kapuas junction. Kapuas upstream (top), Kecil (middle) and Besar (bottom).

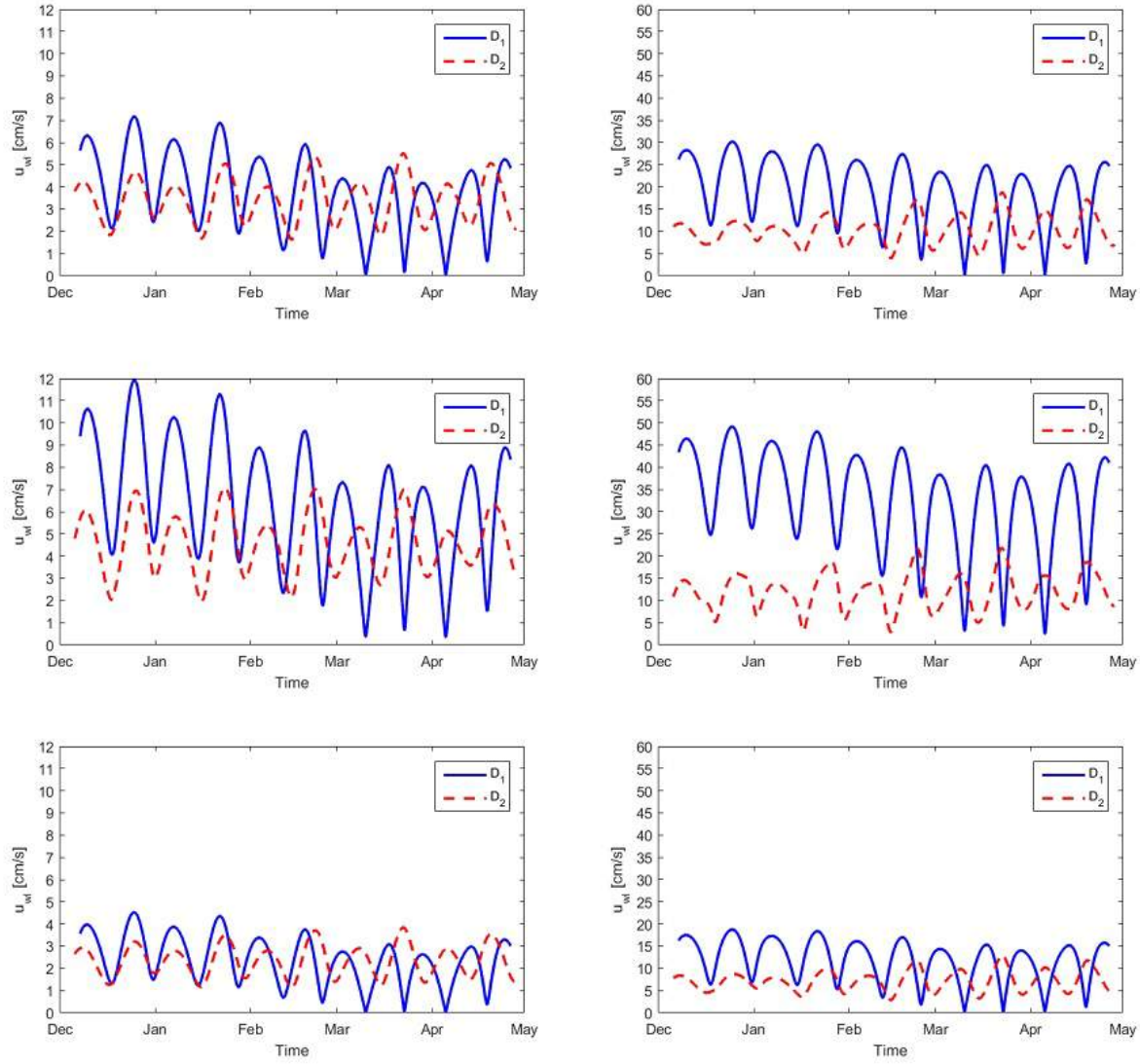

Figure 47: Diurnal (blue solid line) and semidiurnal velocity amplitudes (red dotted line) during high flow (left panel) and low flow (right panel) at the Kubu-Kapuas junction. Kapuas upstream (top), Kubu (middle) and Besar (bottom).

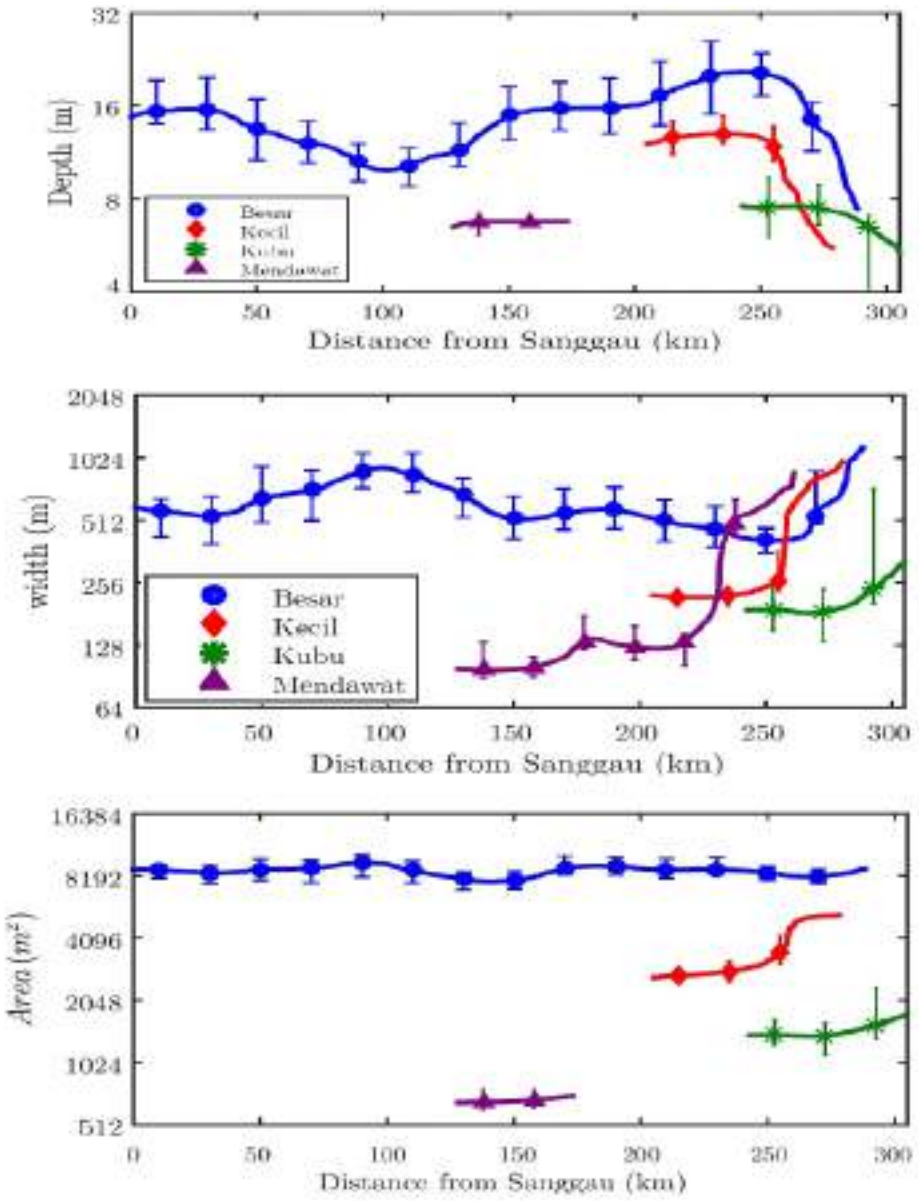

Figure 48: Channel depth, width and area of the Kapuas River (blue dot), Kecil branch (red diamond), Kubu branch (green star) and Mendawat branch (purple triangle). [Kästner et al., 2016].

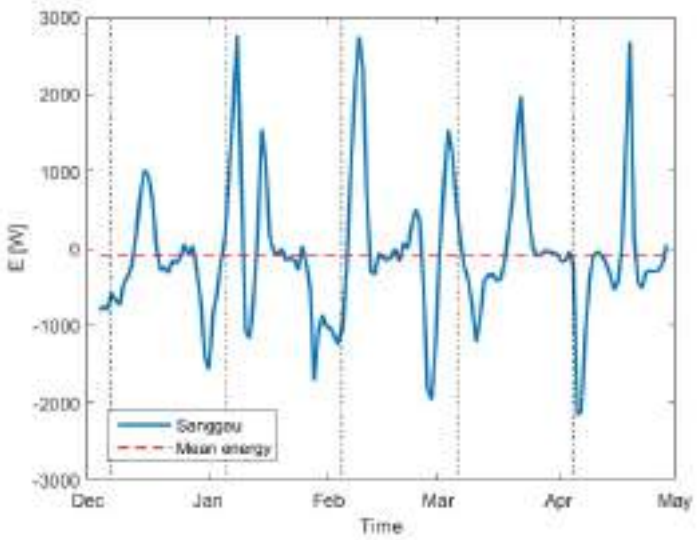

Figure 49: Tidal energy at Sanggau during low flow. Red dashed line indicates the mean tidal energy (∼100[KW]).

Table 10: Amplitudes for diurnal and semidiurnal tidal species and the corresponding tidal ranges at different observation points along the Kecil branch.

Kecil branch	High flow (10000m^3/s)			Low flow (1000m^3/s)		
	D_1 Amplitude [cm]	D_2 Amplitude [cm]	Range [cm]	D_1 Amplitude [cm]	D_2 Amplitude [cm]	Range [cm]
K7	9.61	6.27	28.17	18.70	21.27	71.18
K6	9.16	6.09	26.98	19.06	22.76	76.67
K5	8.77	5.79	25.75	19.16	23.46	80.50
K4	8.52	5.54	24.95	19.02	23.53	81.45
K3	8.38	5.33	24.35	18.80	23.40	81.24
K2	8.31	5.15	23.89	18.60	22.72	79.16
K1b (at sea)	4.46	3.94	17.57	4.37	3.87	17.38
K1 (at sea)	8.40	5.22	24.26	18.39	20.69	73.43

Table 11: Amplitudes for diurnal and semidiurnal tidal species and the corresponding tidal ranges at different observation points along the Kapuas branch.

Kubu branch	High flow (10000m^3/s)			Low flow (1000m^3/s)		
	D_1 Amplitude [cm]	D_2 Amplitude [cm]	Range [cm]	D_1 Amplitude [cm]	D_2 Amplitude [cm]	Range [cm]
A6	15.42	10.16	44.88	23.72	24.95	85.13
A5	20.87	13.93	60.29	29.39	27.61	99.22
A4	26.97	17.82	77.24	34.57	29.28	110.89
A3	30.60	20.47	87.88	37.12	29.09	115.99
A2	32.63	21.69	93.44	38.15	28.15	116.50
A1 (at sea)	35.67	23.37	101.73	39.48	26.94	116.50
A6	15.42	10.16	44.88	23.72	24.95	85.13
A5	20.87	13.93	60.29	29.39	27.61	99.22
A4	26.97	17.82	77.24	34.57	29.28	110.89
A3b	39.20	23.81	110.45	43.35	29.73	127.69
A2b	45.10	26.47	126.87	47.43	29.28	135.79
A1b (at sea)	49.82	28.47	139.97	49.99	28.76	140.72

Table 12: Model input parameters for fifty scenarios derived from Latin Hypercube Sampling technique.

#	Q_{in}	C	d	#	Q_{in}	C	d
Scenario	**[m^3/s]**	**[$m^{1/2}/s$]**	**[m]**	**Scenario**	**[m^3/s]**	**[$m^{1/2}/s$]**	**[m]**
1	4203.03	49.45	0.695	*26*	9011.53	17.82	-0.001
2	5011.27	29.74	-0.157	*27*	9394.23	33.97	-1.07
3	2522.67	39.61	3.04	*28*	5136.64	35.39	0.864
4	5928.18	55.83	-0.822	*29*	4815.63	57.46	3.371
5	7161.55	51.46	0.764	*30*	3908.59	55.5	1.201
6	3561.47	46.86	2.295	*31*	8042.59	66.9	0.072
7	4403.56	43.66	-0.996	*32*	6177.13	58.71	0.252
8	5587.96	64.38	1.07	*33*	5425.12	50.38	0.938
9	4569.08	51.3	-0.13	*34*	6318.95	25.24	0.512
10	8328.52	34.92	0.444	*35*	4121.65	46.36	0.557
11	7558.44	61.85	-1.743	*36*	8660.11	44.86	-1.503
12	4962.1	40.25	0.121	*37*	4645.84	53.66	-0.711
13	6016.91	63.2	2.44	*38*	6461.45	44.55	-0.915
14	1965.47	52.4	1.895	*39*	6836.4	28.33	-0.603
15	2697.52	36.52	-3.182	*40*	2098.21	48.27	-1.463
16	5713.51	41.48	1.262	*41*	5222.15	21.4	-0.376
17	2389.89	68.79	1.418	*42*	5383.38	48.79	-1.828
18	7982.19	54.44	1.545	*43*	5838.83	39.14	-2.687
19	7287.98	26.85	-2.136	*44*	3037.47	22.81	-2.1
20	3451.56	60.27	-0.297	*45*	1729.98	31.08	0.333
21	1117.07	59.37	-1.34	*46*	3232.02	45.77	-0.418
22	6512.55	81.62	-0.678	*47*	4391.81	41.76	-2.372
23	6988.83	72.41	1.013	*48*	3135.18	37.76	-1.214
24	7747.38	42.97	2.091	*49*	3994.34	31.64	-0.513
25	6652.82	33.06	1.64	*50*	3671.68	37.95	0.224

Table 13: Basic statistics of the parameter sample.

Model Parameter	**C**	**Q_{in}**	**d**
	[$m^{1/2}/s$]	**[m^3/s]**	**[m]**
Minimum	17.82	1117	-3.182
1^{st} Quarter	35.67	3731	-0.976
Median	45.32	5179	0.036
Mean	45.76	5220	0.016
3^{rd} Quarter	55.23	6618	0.994
Maximum	81.62	9394	3.371

11 Appendix

Derivation of tidal energy transport across a channel section

The tidal energy flux per unit width [Gill, 1982] can be written as:

$$\overrightarrow{F} = \frac{\rho g H}{T} \int_0^T \zeta \overrightarrow{u} \, \mathrm{d}t \tag{10}$$

Decomposing $\overrightarrow{F}$ and $\overrightarrow{u}$ as binormal vectors,

$$\overrightarrow{F} = F_n \overrightarrow{n} + F_s \overrightarrow{s} \tag{11}$$

$$\overrightarrow{u} = u_n \overrightarrow{n} + u_s \overrightarrow{s} \tag{12}$$

where 'n' indicates the orthogonal direction respect to a cross section line, and 's' the tangent direction. Therefore, the tidal energy per unit width in the orthogonal direction can be expressed as follows:

$$\overrightarrow{F}_n = \frac{\rho g H}{T} \int_0^T \zeta \overrightarrow{u}_n \, \mathrm{d}t \tag{13}$$

The energy flux integrated over the cross section width 'w' can be written as:

$$\overrightarrow{E} = \int_0^w \overrightarrow{F}_n \, \mathrm{d}n = \int_0^w \frac{\rho g H}{T} \int_0^T \zeta \overrightarrow{u}_n \, \mathrm{d}t \, \mathrm{d}n \tag{14}$$

or in the form:

$$\overrightarrow{E} = \frac{\rho g H}{T} \int_0^T \int_0^w \zeta \overrightarrow{u}_n \, \mathrm{d}n \, \mathrm{d}t = \frac{\rho g H}{T} \int_0^T \zeta \int_0^w \overrightarrow{u}_n \, \mathrm{d}n \, \mathrm{d}t \tag{15}$$

Moreover, since DELFT3D-FM® computes the flow velocity as:

$$\overrightarrow{u} = \frac{Q}{A} \tag{16}$$

where 'Q' is the cross section discharge and 'A' the cross section area. The flow velocity can be defined as follows:

$$\overrightarrow{u} = \frac{1}{w} \int_0^w \overrightarrow{u}_n \, \mathrm{d}n \tag{17}$$

Thus, integrating $\overrightarrow{u}$ over the channel width, the total tidal energy across a channel section results:

$$\overrightarrow{E} = \frac{\rho g H}{T} \int_0^T \zeta \overrightarrow{u} w \, \mathrm{d}n = \frac{\rho g H w}{T} \int_0^T \zeta \overrightarrow{u} \, \mathrm{d}n \tag{18}$$

References

Buschman, F., Hoitink, A., Van Der Vegt, M., & Hoekstra, P. (2010). Subtidal flow division at a shallow tidal junction. *Water Resources Research*, *46*(12).

Buschman, F., Vegt, M., Hoitink, A., & Hoekstra, P. (2013). Water and suspended sediment division at a stratified tidal junction. *Journal of Geophysical Research: Oceans*, *118*(3), 1459–1472.

Defant, A. (1961). *Physical oceanography; volume 2*. Pergamon press.

Deltares. (2017). D-flow flexible mesh, user manual [Computer software manual].

Deynoot, G. (2011). *Analytical modelling of salt intrusion in the kapuas estuary*.

Fisher, R. (1992). Statistical methods for research workers. , 66–70.

Godin, G. (1991). Frictional effects in river tides. *Tidal hydrodynamics*, *379*, 402.

Goltenboth, F., Timotius, K. H., Milan, P. P., & Margraf, J. (2006). *Ecology of insular southeast asia: the indonesian archipelago*. Elsevier.

Helton, J. C., & Davis, F. J. (2003). Latin hypercube sampling and the propagation of uncertainty in analyses of complex systems. *Reliability Engineering & System Safety*, *81*(1), 23–69.

Hoitink, A., & Jay, D. A. (2016). Tidal river dynamics: implications for deltas. *Reviews of Geophysics*.

Kernkamp, H. W., Van Dam, A., Stelling, G. S., & de Goede, E. D. (2011). Efficient scheme for the shallow water equations on unstructured grids with application to the continental shelf. *Ocean Dynamics*, *61*(8), 1175–1188.

Kästner, K., & Hoitink, A. (2016). Distributary channels interconnected by u-shaped junctions in the kapuas coastal zone.

Lau, K., & Weng, H. (1995). Climate signal detection using wavelet transform: How to make a time series sing. *Bulletin of the American Meteorological Society*, *76*(12), 2391–2402.

Leonardi, N., Kolker, A. S., & Fagherazzi, S. (2015). Interplay between river discharge and tides in a delta distributary. *Advances in Water Resources*, *80*, 69–78.

Meybeck, M., & Ragu, A. (1995). *River discharges to the oceans: an assessment of suspended solids, major ions and nutrients*. UNEP.

Munk, W. H. (2010). Origin and generation of waves. *Coastal Engineering Proceedings*, *1*(1), 1.

NOAA. (2013). *Tidal current predictions and data - noaa.* Retrieved 2017-01-03, from `https://tidesandcurrents.noaa.gov/faq4.html`

Pugh, D., & Woodworth, P. (2014). *Sea-level science: understanding tides, surges, tsunamis and mean sea-level changes*. Cambridge University Press.

Pugh, D. T. (1996). *Tides, surges and mean sea-level (reprinted with corrections)*. John Wiley & Sons Ltd.

Sassi, M. G., Hoitink, A., de Brye, B., Vermeulen, B., & Deleersnijder, E. (2011). Tidal impact on the division of river discharge over distributary channels in the mahakam delta. *Ocean Dynamics*, *61*(12), 2211–2228.

Tahun. (2003). *Tide tables, indonesian archipelago*. Dinas Hidro-Oseanografi.

Te Chow, V. (1959). *Open channel hydraulics*. McGraw-Hill Book Company, Inc; New York.

Torrence, C., & Compo, G. P. (1998). A practical guide to wavelet analysis. *Bulletin of the American Meteorological society*, *79*(1), 61–78.

Zhong, L., & Li, M. (2006). Tidal energy fluxes and dissipation in the chesapeake bay. *Continental Shelf Research*, *26*(6), 752–770.